On thermomechanical problems in a topology optimisation method based on non-uniform rational basis spline entities

Elisabetta Urso, Marco Montemurro *

Université de Bordeaux, Arts et Métiers Institute of Technology, CNRS, INRA, Bordeaux INP, HESAM Université, I2M UMR 5295, F-33405 Talence, France

Keywords:
Topology optimisation
NURBS
Design-dependent loads
Density-based algorithm
Thermomechanics
Penalisation scheme

A B S T R A C T

This paper presents a new method to deal with thermomechanical topology optimisation (TO) problems based on a pseudo-density algorithm reformulated in the context of Non Uniform Rational Basis Spline (NURBS) entities. Specifically, a NURBS entity is used to represent the topological descriptor, providing an implicit filtering effect thanks to the local support propriety. The problem is formulated in the most general case of inhomogeneous Neumann-Dirichlet boundary conditions and design-dependent thermal sources and thermomechanical loads. In this context, a study on the combined effect of design-dependent heat sources, thermomechanical loads and applied forces and displacements on the optimal topologies is carried out. Furthermore, the influence of the penalisation schemes involved in the definition of the stiffness matrix, conductivity matrix, thermal loads and thermal sources on the optimised topology is investigated through a wide campaign of sensitivity analyses. Finally, sensitivity analyses are also conducted to investigate the influence of the integer parameters of the NURBS entity on the optimised solution. The effectiveness of the approach is tested on 2D and 3D benchmark problems.

1. Introduction

Topology optimisation (TO) methods constitute innovative approaches to design products and components due to their intrinsic ability to find unconventional optimised solutions by starting from scratch. The vast majority of works on TO available in the literature focuses on structural problems subjected to external design-independent loads. In this framework, the goal is to maximise the structural stiffness while respecting a design constraint on the volume: the merit function used to evaluate the stiffness is usually related to the work of external forces, which is equal to twice the strain energy. In the last decades, several approaches for TO have been formulated, but the density-based methods [1,2] and the level set method (LSM) [3–5] constitute the most known and used.

This work focuses exclusively on the former class of methods. Density-based TO algorithms are based on a fictitious density function which varies in the range $]0, 1]$, where the two bounds represent the absence (void phase) and presence (solid phase) of the material within the design domain. In the context of density-based TO algorithms, the convergence towards black and white designs is guaranteed through the introduction of a dedicated penalisation scheme, which aims to avoid meaningless intermediate values of the pseudo-density field, like the solid isotropic material with penalisation (SIMP) [6] or the rational approximation of material properties (RAMP) [7] ones. The success of this method is due to its compactness and efficiency, but some drawbacks have to be considered. Firstly, the topological descriptor relies on the mesh of the finite element (FE) model, hence the boundary of the topology is not available in a computer-aided design (CAD) compatible form at the end of the process. To recover the boundary of the topology, a time-consuming process of reconstruction/reassembly is thus needed. Secondly, dedicated filtering techniques or projection methods must be introduced in the problem formulation to reduce the well-known checkerboard effect and the mesh-dependency of the solution [8,9].

Some of the above issues can be overcome by reformulating the classic density-based TO algorithm in the context of the non-uniform rational basis spline (NURBS) entities [10–12], as done in [13,14]. This method is characterised by some interesting features corresponding to just as many advantages. Firstly, the pseudo-density field is described by a continuous NURBS entity of dimension $D + 1$ (where D is the dimension of the numerical model of the structure), i.e., a purely geometrical entity, which avoids the dependence of the topological descriptor on the mesh of the FE model. In addition this method is fully compatible with CAD software since the topology boundary is available at each iteration, limiting/avoiding post-processing operations to recover the

* Corresponding author.
E-mail addresses: marco.montemurro@ensam.eu, marco.montemurro@u-bordeaux.fr (M. Montemurro).

https://doi.org/10.1016/j.compstruc.2024.107530

Nomenclature

Acronyms

BC	boundary condition
BP	benchmark problem
B-spline	basis spline
CAD	computer-aided design
CNLPP	constrained non-linear programming problem
CP	control point
DC	design case
DDL	design-dependent load
DOF	degree of freedom
FE	finite element
GCMMA	globally-convergent method of moving asymptotes
LSM	level set method
NURBS	non-uniform rational basis spline
RAMP	rational approximation of material properties
SIMP	solid isotropic material with penalisation
TO	topology optimisation

solution boundary [14,15]. Furthermore, the checkerboard effect can be reduced/avoided by exploiting the local support property of the NURBS basis function [12], which constitutes an efficient implicit filter associated with the definition of the NURBS entity.

Nowadays, modern engineering applications in different sectors, such as aerospace, energy and biomedical fields, often require multiphysics (or multi-field) analyses. However, when considering multiphysics analyses, such as thermomechanical, electromechanical or aeroelastic simulations, the loads applied to the structure implicitly depend on the current topology: this aspect significantly increase the complexity of the TO problem. The works on TO problems involving design-dependent loads (DDLs) are scarce and they were initially carried out by Bruyneel and Duysinx [16], who focused on self-weight, pointing out that the problem formulation does not correspond to a natural extension of the classical TO problem with prescribed external loads.

In this context, a class of TO problems involving DDLs is constituted by the thermomechanical problems [17–20]. Thermal strains can be a source of failure for mechanical components operating at high temperatures, requiring structural designs able to reduce the associated effects. An efficient TO framework is hence fundamental for several devices, such as semi-conductors electronics, heat exchangers, turbine blades, cooling systems. In thermomechanical problems, the DDLs depend on the topological descriptor both implicitly and explicitly. Specifically, thermal sources and inertial loads depend explicitly on the topological variables, whereas thermal loads derived from thermal strains depend implicitly on the topological descriptors through the temperature field, which is the outcome of the thermal analysis. Indeed, two different equilibrium systems, one for the thermal problem and one for the structural problem [21–24] are solved by usually considering a weak coupling between the different physics.

The steady-state heat conduction problem constitutes the most simple case in this class of problems and it is examined in different works [25–29]. Zhuang and Xiong [30] have discussed the case with a temperature constraint for transient-state heat conduction. Among the above studies, in [31,32] it is highlighted that the presence of thermal loads increases the complexity of the TO problem. This is related to the choice of the correct penalisation scheme for the tensor describing the physics at the basis of thermomechanical analyses, i.e., elasticity tensor, thermal conductivity tensor and tensor of the coefficients of thermal expansion. Indeed, if the different penalisation schemes are not accurately defined, it is difficult to avoid intermediate density values in the final design because the volume constraint is not active for minimum compliance problem when considering thermomechanical analyses, thus the solution is not located on the boundary of the feasible region. To overcome this problem, Gao and Zhang [33] have introduced a thermal stress coefficient, which can be penalised to control simultaneously the structural stiffness and the DDLs, simplifying the definition of thermomechanical problems. In the same work, a comparison between SIMP and RAMP schemes is performed, demonstrating that better results can be achieved with the latter scheme. Pedersen and Pedersen [34,35] demonstrated the substantial difference between minimum compliance designs and maximum strength designs when thermomechanical analyses are considered, proposing an alternative method to overcome this discrepancy based on the von Mises stress minimisation. In [36], a thermomechanical TO problem with stress constraints is presented, while a study on the penalisation method of a linear transient thermomechanical problem is proposed in [37]. Takezawa et al. [38] conducted a study on topology optimisation of thermoelastic structures with optimisation constraints on both stress and thermal conductivity using the volume of the continuum as a cost function to minimise. A similar study considering von Mises stress constraints is presented by Deaton and Grandhi [36]. Moreover, the evolutionary structural optimisation method has been applied to thermoelastic and heat transfer problems to investigate combined thermal and structural criteria and heat conduction [26], while in [33,39] the bi-directional evolutionary structural optimisation method is used to design heat conducting structures in presence of DDLs. In [40,41], the LSM is used to perform a stiffness design on a structure subjected to an uniform temperature loading. In this context, Liu and Tovar [42] compared two different formulations of the thermoelastic TO problems: compliance minimisation with a constraint on the volume and mass minimisation with a constraint on the maximum displacement. In a recent work, Zhang [43] introduced, firstly, a formulation of the TO problem including a stress constraint, and secondly, a reliability-based method to overcome the issues related to the first formulation, i.e., singularity, local nature of the stress and nonlinear behaviour of stress constraints [44]. The moving morphable void approach has been introduced by Fang et al. [45] to deal with thermoelastic TO problems using basis spline (B-spline) to describe the boundary of the "void" phase in the design domain and its evolution during the optimisation process. Inspired by the aforementioned works, thermomechanical TO problems are formulated and addressed in the framework of the NURBS-density-based TO method in this paper. Specifically, they are formulated, for the first time to the best of the authors' knowledge, by considering the most general case of inhomogeneous Neumann-Dirichlet boundary conditions and the presence of thermal sources depending on the topological descriptor during the thermal analysis. The generalised compliance [46] is considered as a cost function subject to an equality constraint on the volume. To this purpose, suitable interpolation schemes are used to penalise the elasticity matrix, the thermal conductivity matrix, the thermal sources and the vector of the thermal loads. In this context, a wide campaign of sensitivity analyses is carried out to study the influence of the different penalisation schemes and of the integer parameters involved in the definition of the NURBS entity on the optimised topology. Moreover, the numerical framework presented in this paper is coupled with a commercial FE code in order to show its potential and versatility.

The effectiveness of the proposed method is tested on both 2D and 3D benchmark structures.

The paper is organised as follows. An overview on the NURBS density-based method and the mathematical formulation of the thermomechanical TO problems are introduced in Section 2. The penalisation schemes used in this work are presented in Section 3. Numerical results are shown and discussed in Section 4, while Section 5 ends the paper with some concluding remarks and prospects.

Notation Upper-case bold letters and symbols are used to indicate matrices, while lower-case bold letters and symbols indicate column vectors.

2. The NURBS-density-based method

The mathematical background of the NURBS-density-based method in the framework of TO problems of structures subjected to design-independent load is described in detail in [13,46,47]. The main features concerning the approach are summarised in the most general case of 3D problems in the following.

2.1. Design variables

Let $D := \{(x_1, x_2, x_3) \in \mathbb{R}^3 \mid x_j \in [0, L_j],\ j = 1, 2, 3.\}$ be a compact Euclidean space, equipped with the Cartesian orthogonal frame $\mathcal{O}(x_1, x_2, x_3)$, representing the design domain, wherein L_j is the characteristic length of the domain along the x_j axis. In the context of the NURBS-density-based method, for a 3D problem, the topological variable, i.e., is the pseudo-density, is represented by a 4D hyper-surface. The first three coordinates of the hyper-surface are used to represent the design domain, whilst the latter is the pseudo-density, which reads:

$$\rho(\zeta_1, \zeta_2, \zeta_3) = \sum_{i_1=0}^{n_1} \sum_{i_2=0}^{n_2} \sum_{i_3=0}^{n_3} R_{i_1 i_2 i_3}(\zeta_1, \zeta_2, \zeta_3) \rho_{i_1 i_2 i_3}. \tag{1}$$

In Eq. (1), $\rho_{i_1 i_2 i_3}$ is the value of the pseudo-density at the generic control point (CP) of the NURBS entity, while $R_{i_1 i_2 i_3}$ is the piece-wise rational basis function that depends on the Berstein's polynomials $N_{i_k, p_k}(\zeta_k)$ of degree p_k $(k = 1, ..., 3)$ through the relationship:

$$R_{i_1 i_2 i_3} := \frac{\omega_{i_1 i_2 i_3} \prod_{k=1}^{N} N_{i_k, p_k}(\zeta_k)}{\sum_{j_1=0}^{n_1} \cdots \sum_{j_N=0}^{n_N} \prod_{k=1}^{N} N_{j_k, p_k}(\zeta_k) \omega_{j_1 j_2 j_3}}, \tag{2}$$

where $\omega_{i_1 i_2 i_3}$ represents the weight associated with each CP and $\zeta_k \in [0, 1]$ is the k-th parametric coordinate, which reads:

$$\zeta_j = \frac{x_j}{L_j},\ j = 1, 2, 3. \tag{3}$$

The Berstein's polynomials along each parametric direction $N_{i_k, p_k}(\zeta_k)$ are recursively defined over the knot vector $\nu^{(k)}$, and their mathematical form together with the associated algorithm can be found in [12]. For more details on the meaning of the different parameters involved in the definition of NURBS hyper-surface, the interested reader is referred to [12,46].

The set of CPs forms the *control hyper-net* [12], which is composed of a total number of CPs equal to:

$$n_{\mathrm{CP}} := \prod_{i=1}^{N} (n_i + 1). \tag{4}$$

The shape of the NURBS entity is influenced by several parameters, of which only the pseudo-density values at the CPs and the associated weights are considered as *design variables* and stored in the arrays $\boldsymbol{\xi}_1$ and $\boldsymbol{\xi}_2$:

$$\boldsymbol{\xi}_1^{\mathrm{T}} := \{\rho_{000}, ..., \rho_{n_1 n_2 n_3}\},\ \boldsymbol{\xi}_2^{\mathrm{T}} := \{\omega_{000}, ..., \omega_{n_1 n_2 n_3}\},\ \boldsymbol{\xi}_1, \boldsymbol{\xi}_2 \in \mathbb{R}^{n_{\mathrm{CP}}}. \tag{5}$$

According to Eq. (5), the number of design variables is at most $n_{\mathrm{var}} = 2n_{\mathrm{CP}}$ in the case of NURBS hyper-surfaces. The remaining parameters are referred to as *design parameters* and are set *a priori* at the beginning of the optimisation process. These parameters consist of the degrees of the Bernstein polynomials, the number of control CPs and the knot vector components. Some general rules have been provided in [13,14,46] to define these quantities, specifically, the inner components of the knot vectors are evenly distributed in the interval $[0, 1]$. The degree and the number of CPs along each parameter direction of the NURBS entity are defined to satisfy the minimum length scale constraint (imposed by the minimum dimension that can be manufactured with the chosen process) according to the guidelines provided in [48]. Basically, the higher the number of CPs (or the lower the degrees), the smaller the local support of the NURBS entity, and thus thin topological features can be obtained.

For TO problems, the number of variables is usually high, so performing a numerical evaluation of the gradient of objective and constraint functions through finite differences is not recommended. Thus, deriving the formal expression of the gradient of physical requirements included in the problem formulation is a mandatory task to accelerate the optimisation process. In the context of the NURBS density-based method, the derivation of the formal expression of the gradient of the physical requirements is achieved by exploiting the local support property of Bernstein's polynomials [12,46]. The local support of the generic CP reads:

$$S_\tau = S_{i_1 i_2 i_3} = [\nu_{i_1}^{(1)}, \nu_{i_1+p_1+1}^{(1)}[\times[\nu_{i_2}^{(2)}, \nu_{i_2+p_2+1}^{(2)}[\times[\nu_{i_3}^{(3)}, \nu_{i_3+p_3+1}^{(3)}[\,, \tag{6}$$

where $\nu^{(j)}$ is the generic component of the knot vector along the j-th parametric direction and the triplet (i_1, i_2, i_3) identifies a CP or a weight and can be replaced by a linear index τ defined as:

$$\tau = 1 + i_1 + (i_2 - 1)(n_1 + 1) + (i_3 - 1)(n_1 + 1)(n_2 + 1). \tag{7}$$

2.2. Cost function

When thermomechanical loads are applied to the structure in the general case of non-zero Neumann-Dirichlet BCs [46], two governing equations are involved in the formulation of the TO problem. Specifically, this paper considers only weak coupling between thermal and structural analyses. In this context, the thermal problem is solved first and the resulting temperature field is then imported into the structural analysis to evaluate the thermal strains and to determine the displacement field. Regarding the thermal problem, only heat conduction problems in steady state regime are considered. The governing equation of the thermal equilibrium reads:

$$\hat{\mathbf{K}}_\theta \hat{\boldsymbol{\theta}} = \hat{\boldsymbol{\psi}},\quad \hat{\boldsymbol{\theta}}, \hat{\boldsymbol{\psi}} \in \mathbb{R}^{\hat{N}_{\theta\mathrm{DOF}}}, \hat{\mathbf{K}}_\theta \in \mathbb{R}^{\hat{N}_{\theta\mathrm{DOF}} \times \hat{N}_{\theta\mathrm{DOF}}} \tag{8}$$

where $\hat{N}_{\theta\mathrm{DOF}}$ is the overall number of thermal degrees of freedom (DOFs), i.e., the nodal temperatures, before the application of BCs, $\hat{\mathbf{K}}_\theta$ is the non-reduced thermal conductivity matrix, while $\hat{\boldsymbol{\theta}}$ and $\hat{\boldsymbol{\psi}}$ are the vectors of nodal temperatures and the nodal thermal loads, respectively. After applying BCs and reordering DOFs, Eq. (8) can be rewritten as:

$$\begin{bmatrix} \mathbf{K}_\theta & \mathbf{K}_{\theta\mathrm{BC}} \\ \mathbf{K}_{\theta\mathrm{BC}}^{\mathrm{T}} & \tilde{\mathbf{K}}_\theta \end{bmatrix} \begin{Bmatrix} \boldsymbol{\theta} \\ \boldsymbol{\theta}_{\mathrm{BC}} \end{Bmatrix} = \begin{Bmatrix} \boldsymbol{\psi} \\ \boldsymbol{\psi}_{\mathrm{BC}} \end{Bmatrix}, \tag{9}$$

with:

$$\begin{aligned}
&\boldsymbol{\theta} := \mathfrak{R}\left(\hat{\boldsymbol{\theta}}, \mathcal{I}_{\theta\mathrm{BC}}\right),\ \boldsymbol{\psi} := \mathfrak{R}\left(\hat{\boldsymbol{\psi}}, \mathcal{I}_{\theta\mathrm{BC}}\right) \\
&\boldsymbol{\theta}_{\mathrm{BC}} := \mathfrak{R}\left(\hat{\boldsymbol{\theta}}, \mathcal{I}_\theta\right),\ \boldsymbol{\psi}_{\mathrm{BC}} := \mathfrak{R}\left(\hat{\boldsymbol{\psi}}, \mathcal{I}_\theta\right), \\
&\mathbf{K}_\theta := \mathfrak{R}\left(\hat{\mathbf{K}}_\theta, \mathcal{I}_{\theta\mathrm{BC}}, \mathcal{I}_{\theta\mathrm{BC}}\right),\ \mathbf{K}_{\theta\mathrm{BC}} := \mathfrak{R}\left(\hat{\mathbf{K}}_\theta, \mathcal{I}_{\theta\mathrm{BC}}, \mathcal{I}_\theta\right), \\
&\tilde{\mathbf{K}}_\theta := \mathfrak{R}\left(\hat{\mathbf{K}}_\theta, \mathcal{I}_\theta, \mathcal{I}_\theta\right), \\
&\boldsymbol{\theta}, \boldsymbol{\psi} \in \mathbb{R}^{N_{\theta\mathrm{DOF}}},\ \boldsymbol{\theta}_{\mathrm{BC}}, \boldsymbol{\psi}_{\mathrm{BC}} \in \mathbb{R}^{N_{\theta\mathrm{BC}} \times N_{\theta\mathrm{BC}}}, \\
&\mathbf{K}_\theta \in \mathbb{R}^{N_{\theta\mathrm{DOF}} \times N_{\theta\mathrm{DOF}}},\ \mathbf{K}_{\theta\mathrm{BC}} \in \mathbb{R}^{N_{\theta\mathrm{DOF}} \times N_{\theta\mathrm{BC}} \times N_{\theta\mathrm{BC}}}, \\
&\tilde{\mathbf{K}}_\theta \in \mathbb{R}^{N_{\theta\mathrm{BC}} \times N_{\theta\mathrm{BC}}} \times N_{\theta\mathrm{BC}} \times N_{\theta\mathrm{BC}},
\end{aligned} \tag{10}$$

where $\mathfrak{R}$ is the operator introduced in [46] which returns the matrix $\mathfrak{M} := \mathfrak{R}\left(\hat{\mathfrak{M}}, \mathcal{R}, \mathcal{C}\right)$ obtained by deleting the rows corresponding to the indices belonging to the set $\mathcal{R}$ and the columns corresponding to indices belonging to the set $\mathcal{C}$. In the above formula, the sets $\mathcal{I}_\theta \subset \{i \mid 1 \le i \le \hat{N}_{\theta\mathrm{DOF}}\}$ and $\mathcal{I}_{\theta\mathrm{BC}} \subset \{i \mid 1 \le i \le \hat{N}_{\theta\mathrm{DOF}}\}$ are two generic sets of indices such that: $\mathcal{I}_\theta \cap \mathcal{I}_{\theta\mathrm{BC}} = \varnothing$, $\mathrm{meas}\left(\mathcal{I}_\theta\right) = N_{\theta\mathrm{DOF}}$, $\mathrm{meas}\left(\mathcal{I}_{\theta\mathrm{BC}}\right) = N_{\theta\mathrm{BC}}$ and $N_{\theta\mathrm{DOF}} + N_{\theta\mathrm{BC}} = \hat{N}_{\theta\mathrm{DOF}}$ (i.e., $N_{\theta\mathrm{BC}}$ is the number of imposed temperatures, whilst $N_{\theta\mathrm{DOF}}$ is the number of unknown temperatures).

In Eq. (9), $\boldsymbol{\theta}$ and $\boldsymbol{\theta}_{\mathbf{BC}}$ are the unknown and prescribed temperatures, respectively, $\boldsymbol{\psi}$ is the vector of external thermal loads, whilst $\boldsymbol{\psi}_{\mathrm{BC}}$ is the vector of nodal thermal reactions on the nodes where temperatures are imposed. $\mathbf{K}_{\theta}$, $\mathbf{K}_{\theta\mathrm{BC}}$ and $\tilde{\mathbf{K}}_{\theta}$ are the thermal conductivity matrices of the FE model after applying BCs and reordering DOFs.

In the context of the TO method, based on the pseudo-density, the latter affects the element thermal conductivity matrix and, accordingly, the global thermal conductivity matrix of the structure as follows:

$$\begin{aligned}&\hat{\mathbf{K}}_{\theta} := \sum_{e=1}^{N_e} \phi_{K_{\theta}}\left(\rho_e\right) \hat{\mathbf{L}}_{\theta e}^{\mathrm{T}} \mathbf{K}_{\theta e}^{0} \hat{\mathbf{L}}_{\theta e} = \sum_{e=1}^{N_e} \hat{\mathbf{L}}_{\theta e}^{\mathrm{T}} \mathbf{K}_{\theta e} \hat{\mathbf{L}}_{\theta e},\\ &\mathbf{K}_{\theta e}^{0}, \mathbf{K}_{\theta e} \in \mathbb{R}^{N_{\theta\mathrm{DOF},e} \times N_{\theta\mathrm{DOF},e}},\ \hat{\mathbf{L}}_{\theta e} \in \mathbb{R}^{N_{\theta\mathrm{DOF},e} \times \hat{N}_{\theta\mathrm{DOF}}},\end{aligned} \tag{11}$$

where ρ_e is the pseudo-density of Eq. (1) computed at the centroid of the generic element, whilst $\phi_{K_{\theta}}\left(\rho_e\right)$ is a suitable interpolation function used to penalise the element thermal conductivity matrix (see Section 3). N_e is the total number of elements and $N_{\theta\mathrm{DOF},e}$ is the number of thermal DOFs of the generic element. In Eq. (11), $\mathbf{K}_{\theta e}^{0}$ and $\mathbf{K}_{\theta e}$ are the non-penalised and the penalised thermal conductivity matrices of element e, expressed in the global reference frame of the FE model, whilst $\hat{\mathbf{L}}_{\theta e}$ is the connectivity matrix of element e relating the nodal temperatures at the element-level to their counterparts at the structure-level:

$$\boldsymbol{\theta}_e = \hat{\mathbf{L}}_{\theta e} \hat{\boldsymbol{\theta}}, \tag{12}$$

where $\boldsymbol{\theta}_e \in \mathbb{R}^{N_{\theta\mathrm{DOF},e}}$ is the vector of nodal temperatures of the generic element. The vector of the external thermal loads, in the most general case, can be expressed as:

$$\boldsymbol{\psi} := \boldsymbol{\psi}_0 + \boldsymbol{\psi}_{\mathrm{DD}}\left(\rho\left(\mathbf{x}\right)\right), \tag{13}$$

where $\boldsymbol{\psi}_0$ represents the vector of design-independent thermal loads, while $\boldsymbol{\psi}_{\mathrm{DD}}\left(\rho\left(\mathbf{x}\right)\right)$ is the vector of design-dependent thermal loads, which reads:

$$\begin{aligned}&\boldsymbol{\psi}_{\mathrm{DD}}(\rho) := \sum_{e=1}^{N_e} \phi_{\psi}\left(\rho_e\right) \mathbf{L}_{\theta e}^{\mathrm{T}} \boldsymbol{\psi}_{\mathrm{DDe}}^{0} \quad \mathbf{L}_{\theta e} = \Re\left(\hat{\mathbf{L}}_{\theta e}, \varnothing, \mathcal{I}_{\theta\mathrm{BC}}\right),\\ &\mathbf{L}_{\theta e} \in \mathbb{R}^{N_{\theta\mathrm{DOF},e} \times N_{\theta,\mathrm{DOF}}},\end{aligned} \tag{14}$$

where $\boldsymbol{\psi}_{\mathrm{DDe}}^{0} \in \mathbb{R}^{N_{\theta\mathrm{DOF},e}}$ is the vector of design-dependent thermal loads of the element and $\phi_{\psi}\left(\rho_e\right)$ is the associated penalisation function (see Section 3). Regarding the structural analysis, the governing equation of the static equilibrium reads:

$$\hat{\mathbf{K}}\hat{\mathbf{u}} = \hat{\mathbf{f}},\ \hat{\mathbf{u}}, \hat{\mathbf{f}} \in \mathbb{R}^{\hat{N}_{\mathrm{DOF}}},\ \hat{\mathbf{K}} \in \mathbb{R}^{\hat{N}_{\mathrm{DOF}} \times \hat{N}_{\mathrm{DOF}}}, \tag{15}$$

where $\hat{N}_{\mathrm{DOF}}$ is the overall number of structural DOFs before the application of BCs, $\hat{\mathbf{K}}$ is the non-reduced (singular) stiffness matrix of the FE model, while $\hat{\mathbf{f}}$ and $\hat{\mathbf{u}}$ are the vectors of the generalised external nodal forces and displacements, respectively. After applying BCs and reordering DOFs, the above formula can be expressed as:

$$\begin{bmatrix} \mathbf{K} & \mathbf{K}_{\mathrm{BC}} \\ \mathbf{K}_{\mathrm{BC}}^{\mathrm{T}} & \tilde{\mathbf{K}} \end{bmatrix} \begin{Bmatrix} \mathbf{u} \\ \mathbf{u}_{\mathrm{BC}} \end{Bmatrix} = \begin{Bmatrix} \mathbf{f} \\ \mathbf{r} \end{Bmatrix}, \tag{16}$$

with:

$$\begin{aligned}&\mathbf{u} := \Re\left(\hat{\mathbf{u}}, \mathcal{I}_{\mathrm{BC}}\right),\ \mathbf{f} := \Re\left(\hat{\mathbf{f}}, \mathcal{I}_{\mathrm{BC}}\right)\\ &\mathbf{u}_{\mathrm{BC}} := \Re\left(\hat{\mathbf{u}}, \mathcal{I}_{\mathrm{U}}\right),\ \mathbf{r} := \Re\left(\hat{\mathbf{f}}, \mathcal{I}_{\mathrm{U}}\right),\\ &\mathbf{K} := \Re\left(\hat{\mathbf{K}}, \mathcal{I}_{\mathrm{BC}}, \mathcal{I}_{\mathrm{BC}}\right),\ \mathbf{K}_{\mathrm{BC}} := \Re\left(\hat{\mathbf{K}}, \mathcal{I}_{\mathrm{BC}}, \mathcal{I}_{\mathrm{U}}\right),\\ &\tilde{\mathbf{K}} := \Re\left(\hat{\mathbf{K}}, \mathcal{I}_{\mathrm{U}}, \mathcal{I}_{\mathrm{U}}\right),\ \mathbf{u}, \mathbf{f} \in \mathbb{R}^{N_{\mathrm{DOF}}},\ \mathbf{u}_{\mathrm{BC}}, \mathbf{r} \in \mathbb{R}^{N_{\mathrm{BC}}},\\ &\mathbf{K} \in \mathbb{R}^{N_{\mathrm{DOF}} \times N_{\mathrm{DOF}}},\ \mathbf{K}_{\mathrm{BC}} \in \mathbb{R}^{N_{\mathrm{DOF}} \times N_{\mathrm{BC}}},\ \tilde{\mathbf{K}} \in \mathbb{R}^{N_{\mathrm{BC}} \times N_{\mathrm{BC}}}.\end{aligned} \tag{17}$$

In Eq. (16), $\mathbf{u}$ and $\mathbf{u}_{\mathrm{BC}}$ are the unknown and prescribed displacements, respectively, $\mathbf{f}$ is the vector of generalised external nodal forces, whilst $\mathbf{r}$ is the vector of nodal reactions on the nodes where BCs on generalised displacements are imposed. $\mathbf{K}$, $\mathbf{K}_{\mathrm{BC}}$ and $\tilde{\mathbf{K}}$ are the stiffness matrices of the FE model after applying BCs and reordering DOFs. $\mathcal{I}_{\mathrm{U}} \subset \{i \mid 1 \leq i \leq \hat{N}_{\mathrm{DOF}}\}$ and $\mathcal{I}_{\mathrm{BC}} \subset \{i \mid 1 \leq i \leq \hat{N}_{\mathrm{DOF}}\}$ are two sets of indices such that: $\mathcal{I}_{\mathrm{U}} \cap \mathcal{I}_{\mathrm{BC}} = \varnothing$, $\mathrm{meas}\left(\mathcal{I}_{\mathrm{U}}\right) = N_{\mathrm{DOF}}$, $\mathrm{meas}\left(\mathcal{I}_{\mathrm{BC}}\right) = N_{\mathrm{BC}}$ and $N_{\mathrm{DOF}} + N_{\mathrm{BC}} = \hat{N}_{\mathrm{DOF}}$ (i.e., N_{BC} is the number of imposed displacements , whilst N_{DOF} is the number of unknown DOFs).

The global stiffness matrix of the FE model reads:

$$\begin{aligned}&\hat{\mathbf{K}} := \sum_{e=1}^{N_e} \phi_K\left(\rho_e\right) \hat{\mathbf{L}}_e^{\mathrm{T}} \mathbf{K}_e^{0} \hat{\mathbf{L}}_e = \sum_{e=1}^{N_e} \hat{\mathbf{L}}_e^{\mathrm{T}} \mathbf{K}_e \hat{\mathbf{L}}_e,\\ &\mathbf{K}_e^{0}, \mathbf{K}_e \in \mathbb{R}^{N_{\mathrm{DOF},e} \times N_{\mathrm{DOF},e}},\ \hat{\mathbf{L}}_e \in \mathbb{R}^{N_{\mathrm{DOF},e} \times \hat{N}_{\mathrm{DOF}}},\end{aligned} \tag{18}$$

where $\phi_K\left(\rho_e\right)$ is the penalisation function used for the element stiffness matrix (see Section 3) and $N_{\mathrm{DOF},e}$ is the number of DOFs of the generic element. In Eq. (18), $\mathbf{K}_e^{0}$ and $\mathbf{K}_e$ are the non-penalised and the penalised stiffness matrices of element e, expressed in the global reference frame of the FE model, whilst $\hat{\mathbf{L}}_e$ is the connectivity matrix of element e relating the DOFs at the element-level to their counterparts at the structure-level:

$$\mathbf{u}_e = \hat{\mathbf{L}}_e \hat{\mathbf{u}}, \tag{19}$$

where $\mathbf{u}_e \in \mathbb{R}^{N_{\mathrm{DOF},e}}$ is the vector of nodal displacements of the generic element.

When considering thermomechanical analyses with weak coupling, the vector of applied nodal forces implicitly depends on the topological descriptor through the temperature field, i.e., $\hat{\boldsymbol{\theta}} = \hat{\boldsymbol{\theta}}(\rho(\mathbf{x}))$. Therefore, for TO problems including thermomechanical analysis the vector $\mathbf{f}$ reads:

$$\mathbf{f} = \mathbf{f}_0 + \mathbf{f}_{\hat{\theta}}\left(\hat{\boldsymbol{\theta}}\right), \tag{20}$$

where $\mathbf{f}_0$ and $\mathbf{f}_{\hat{\theta}}$ are the design-independent and design-dependent forces, respectively.

The design-dependent term can be rewritten as:

$$\mathbf{f}_{\hat{\theta}} = \sum_{e=1}^{N_e} \phi_{\theta}\left(\rho_e\right) \mathbf{L}_e^{\mathrm{T}} \mathbf{f}_{\hat{\theta}e}, \quad \mathbf{f}_{\hat{\theta}e} \in \mathbb{R}^{N_{\mathrm{DOF},e}}, \tag{21}$$

where $\phi_{\theta}\left(\rho_e\right)$ is the function used to penalise the thermomechanical load (see Section 3), while $\mathbf{f}_{\hat{\theta}\mathrm{e}}$ is defined as:

$$\mathbf{f}_{\hat{\theta}\mathrm{e}} := \int_{V_e} \mathbf{B}^{\mathrm{T}} \mathbf{C} \boldsymbol{\varepsilon}_{\mathrm{th}} \mathrm{d}V, \tag{22}$$

where $\mathbf{B} \in \mathbb{R}^{6 \times N_{\mathrm{DOF}}^{e}}$ and V_e are the matrix of partial derivatives of the element shape functions, and the volume of the element, respectively. $\mathbf{C} \in \mathbb{R}^{6 \times 6}$ is the elasticity matrix, of the material (Voigt's notation), while $\boldsymbol{\varepsilon}_{\mathrm{th}} \in \mathbb{R}^{6}$ is the thermal strain vector defined as follows:

$$\begin{aligned}\boldsymbol{\varepsilon}_{\mathrm{th},e} &= \boldsymbol{\chi}_e(\theta\left(\mathbf{x}\right) - \theta_{\mathrm{ref}}) = \boldsymbol{\chi}_e\left(\mathbf{N}\boldsymbol{\theta}_e - \theta_{\mathrm{ref}}\right)\\ &= \boldsymbol{\chi}_e\left(\mathbf{N}\hat{\mathbf{L}}_{\theta e}\hat{\boldsymbol{\theta}} - \theta_{\mathrm{ref}}\right), \quad \boldsymbol{\chi}_e \in \mathbb{R}^{6},\end{aligned} \tag{23}$$

where θ_{ref} is the reference temperature used in the analysis, $\boldsymbol{\chi}_e$ is the vector of thermal expansion coefficients of the material (Voigt's notation) for the generic element, whilst $\mathbf{N} \in \mathbb{R}^{1 \times N_{\theta\mathrm{DOF},e}}$ is the matrix of the element shape functions (for the thermal analysis). Injecting Eq. (23) in Eq. (22), $\mathbf{f}_{\hat{\theta}\mathrm{e}}$ can be expressed as:

$$\mathbf{f}_{\hat{\theta}e} = \hat{\mathbf{a}}_e \hat{\boldsymbol{\theta}} + \mathbf{b}_e, \tag{24}$$

where

$$\hat{\mathbf{a}}_e = \int_{\Omega_e} \mathbf{B}^{\mathrm{T}} \mathbf{C} \boldsymbol{\chi} \mathbf{N} \mathrm{d}\Omega \hat{\mathbf{L}}_{\theta e}, \quad \hat{\mathbf{a}}_e \in \mathbb{R}^{N_{\mathrm{DOF},e} \times \hat{N}_{\theta\mathrm{DOF}}}, \tag{25}$$

and:

$$\mathbf{b}_e = -\theta_{\text{ref}} \int_{\Omega_e} \mathbf{B}^{\mathrm{T}} \mathbf{C} \boldsymbol{\chi} \mathrm{d}\Omega, \quad \mathbf{b}_e \in \mathbb{R}^{N_{\text{DOF}\,e}}. \tag{26}$$

The formulation of the TO problem considered in this paper deals with the maximisation of the structural stiffness subject to a constraint on the total volume of the design domain [2,6]. In the literature, the work of external forces is often used as a measure of the structural stiffness. As pointed out in [46], under inhomogeneous Neumann-Dirichlet BCs, the work of external forces cannot be used as a measure of structural stiffness, but the generalised compliance must be considered, which can be expressed as follows:

$$C = \mathbf{f}^{\mathrm{T}}\mathbf{u} - \mathbf{u}_{\text{BC}}^{\mathrm{T}}\mathbf{r}. \tag{27}$$

Regarding the gradient of C, consider the following proposition.

Proposition 2.1. *Consider a deformable continuum subject to given boundary conditions, in terms of temperature field, thermal loads, forces and displacement fields. If the prescribed temperatures and displacements do not depend on the pseudo-density field, the gradient of the generalised compliance reads:*

$$\begin{cases} \dfrac{\partial C}{\partial \xi_{i\tau}} = \displaystyle\sum_{e \in S_\tau} \frac{\partial \rho_e}{\partial \xi_{i\tau}} \left[\frac{2}{\phi_{\theta e}} \frac{\partial \phi_{\theta e}}{\partial \rho_e} w_{\theta e}^{\text{ext}} - \frac{1}{\phi_{Ke}} \frac{\partial \phi_{Ke}}{\partial \rho_e} w_e \right. \\ \qquad \left. + \boldsymbol{\lambda}_e^{\mathrm{T}} \left(\dfrac{1}{\phi_{K_\theta e}} \dfrac{\partial \phi_{K_\theta e}}{\partial \rho_e} \boldsymbol{\psi}_e - \dfrac{\partial \phi_{\psi e}}{\partial \rho_e} \boldsymbol{\psi}_{\text{DDe}}^0 \right) \right], \\ i = 1,2, \ \tau = 1, \cdots, n_{\text{CP}}, \\ \mathbf{K}_\theta \boldsymbol{\lambda} = \mathbf{d}, \end{cases} \tag{28}$$

where the internal work of the generic element, i.e., w_e, and the work of the thermomechanical forces acting on the generic element, i.e., $w_{\theta e}^{\text{ext}}$, are defined as

$$w_e := \mathbf{u}_e^{\mathrm{T}} \mathbf{K}_e \mathbf{u}_e, \tag{29}$$

$$w_{\theta e}^{\text{ext}} := \phi_{\theta e} \mathbf{u}_e^{\mathrm{T}} \mathbf{f}_{\theta e} \tag{30}$$

whilst $\boldsymbol{\psi}_e$ represents the vector of thermal reactions of the generic element that reads

$$\boldsymbol{\psi}_e := \phi_{K_\theta e} \mathbf{K}_{\theta e} \boldsymbol{\theta}_e. \tag{31}$$

A proof of Proposition 2.1 is provided in Appendix A.

Remark 2.1. The generalised compliance is not a self-adjoint functional when thermomechanical analyses (with or without design-dependent thermal loads) are considered. To this end, to assess its gradient, the adjoint system (thermal analysis) of Eq. (28) must be solved, wherein the expression of vector $\mathbf{d}$ is:

$$\mathbf{d} = -2 \sum_{e=1}^{N_e} \phi_{\theta e} \mathbf{a}_e^{\mathrm{T}} \mathbf{u}_e, \tag{32}$$

where $\mathbf{a}_e$ can be derived from Eq. (27) as follows

$$\mathbf{a}_e = \Re\left(\hat{\mathbf{a}}_e, \varnothing, \mathcal{I}_{\theta \text{BC}}\right) = \int_{\Omega_e} \mathbf{B}^{\mathrm{T}} \mathbf{C} \boldsymbol{\alpha} \mathbf{N} \mathrm{d}\Omega \mathbf{L}_{\theta e}. \tag{33}$$

Remark 2.2. In Eq. (28), the terms $\phi_{\theta e}$, ϕ_{Ke}, $\phi_{K_\theta e}$ and $\phi_{\psi e}$ are the penalisation functions used for thermomechanical forces, stiffness matrix, thermal conductivity stiffness matrix and thermal loads of the element, whereas the term $\dfrac{\partial \rho_e}{\partial \xi_{i\tau}}$ is the partial derivative of the NURBS entity that can be found in [46].

2.3. Constraint function

In this work, the lightness of the structure is considered as a design requirement, which is expressed by a constraint on the volume of the structure. The volume of the continuum is penalised as follows:

$$V = \sum_{e=1}^{N_e} \rho_e V_e. \tag{34}$$

Its gradient is obtained by differentiating Eq. (34):

$$\frac{\partial V}{\partial \xi_{ij}} = \sum_{e \in S_j} V_e \frac{\partial \rho_e}{\partial \xi_{ij}}, \quad i = 1,2, \quad j = 1, \ldots, n_{\text{CP}}. \tag{35}$$

Thus, the associated constraint function reads:

$$g(\xi_1, \xi_2) := \frac{V}{V_{\text{ref}}} - \gamma, \tag{36}$$

where V_{ref} is a reference value of the volume and γ is the prescribed volume fraction.

2.4. Problem formulation

The TO problem under thermomechanical loads can now be correctly formalised as a constrained nonlinear programming problem (CNLPP) as follows:

$$\min_{\xi_1, \xi_2} \frac{C(\xi_1, \xi_2)}{|C_{\text{ref}}|}, \text{ subject to: } \begin{cases} \hat{\mathbf{K}}\hat{\mathbf{u}} = \hat{\mathbf{f}}, \\ \hat{\mathbf{K}}_\theta \hat{\boldsymbol{\theta}} = \hat{\boldsymbol{\psi}}, \\ g(\xi_1, \xi_2) = 0, \\ \xi_{1j} \in [\rho_{\text{LB}}, \rho_{\text{UB}}], \ \xi_{2j} \in [\omega_{\text{LB}}, \omega_{\text{UB}}], \\ j = 1, \ldots, n_{\text{CP}}, \end{cases} \tag{37}$$

where C_{ref} is the reference value of the compliance of the structure (the absolute value is considered in the above formula because the compliance is not a positive definite function when considering inhomogeneous Neumann-Dirichlet BCs), ρ_{LB} and ρ_{UB} are lower and upper bounds for the pseudo-density evaluated at each CP, while ω_{LB} and ω_{UB} are the bounds for the weights.
In order to prevent singularity problems related to the thermal conductivity and stiffness matrices of the structure, the lower bound of the pseudo-density must be strictly positive.

3. The penalisation schemes

An essential step in the problem definition is the choice of the penalisation scheme for the thermomechanical forces, the distributed thermal loads, the thermal conductivity matrix and the elasticity matrix. The choice of the penalisation scheme influences the optimised designs, the convergence of the problem and can affect the problem through parasitic effects and singularity phenomena [31,32]. However, choosing the right combination of appropriate penalty schemes is not a trivial task.

The first penalisation scheme considered in this work is the well-known SIMP scheme [2,6,49], which reads:

$$\phi_i(\rho_e) = \rho_e^\alpha, \ \frac{\partial \phi_i(\rho_e)}{\partial \rho_e} = \alpha \rho_e^{\alpha - 1}, \ i = K, K_\theta, \theta, \psi, \tag{38}$$

where α is the penalty parameter: the higher α, the stronger the penalisation of intermediate pseudo-density values. In this study it varies between 0 and 3, depending on the vector/matrix to which the penalisation is applied. The second penalty scheme is the RAMP, which was introduced by Stolpe and Svanberg [7] and guarantees finite value of the partial derivative when the pseudo-density goes to zero. The RAMP scheme can be expressed as:

Table 1
GCMMA algorithm parameters.

Parameter	Value
move	0.1
albefa	0.1
Stop Criterion	**Value**
Maximum n. of function evaluations	10000
Maximum n. of iterations	N_{iter}^{max}
Tolerance on objective function	10^{-20}
Tolerance on constraints	10^{-6}
Tolerance on input variables change	10^{-6}
Tolerance on Karush –Kuhn –Tucker norm	10^{-6}

$$\phi_i(\rho_e) = \frac{\rho_e}{1+q(1-\rho_e)}, \quad \frac{\partial \phi_i(\rho_e)}{\partial \rho_e} = \frac{1+q}{\left[1+q\left(1-\rho_e\right)\right]^2}, \quad i = K, K_\theta, \theta, \psi, \tag{39}$$

where q is the penalisation parameter, which varies between 4 and 8 in this study. The last penalisation scheme considered in this paper is a modified version of the linear penalisation scheme, which reads:

$$\phi_i\left(\rho_e\right) = \left(\frac{\rho_e - \rho_{\mathrm{LB}}}{1-\rho_{\mathrm{LB}}}\right)^{\beta}, \quad \frac{\partial \phi_i\left(\rho_e\right)}{\partial \rho_e} = \frac{\beta}{1-\rho_{\mathrm{LB}}}\left(\frac{\rho_e - \rho_{\mathrm{LB}}}{1-\rho_{\mathrm{LB}}}\right)^{\beta-1} \tag{40}$$
$$i = K, K_\theta, \theta, \psi.$$

This scheme has been introduced in [50] to avoid singularity of the solution when considering inertial loads. In fact, at low pseudo-density values, the standard linear penalty scheme cannot be used in combination with a SIMP penalty scheme on the stiffness matrix of the element. This occurs because, as ρ tends to zero, the penalised stiffness matrix of the generic element goes to zero faster than the DDLs of the element.

Conversely, using the penalty scheme of Eq. (40), when $\rho_e = \rho_{\mathrm{LB}}$ the DDLs are exactly zero, regardless of the penalisation scheme used for the stiffness matrix. For the numerical analyses presented in this paper, the parameter β has been set as $\beta = 1$.

4. Numerical results

In this section, the effectiveness of the method is tested on 2D and 3D benchmark structures by considering thermomechanical analyses.

The results presented in the following are obtained using the NURBS-density-based algorithm developed in previous works [13,14]. The globally-convergent method of moving asymptotes (GCMMA) algorithm [51] is used to solve the CNLPP of Eq. (37). The parameters tuning the behaviour of the GCMMA algorithm are listed in Table 1.

The pseudo-density value at CPs varies between $\rho_{\mathrm{LB}} = 10^{-3}$ and $\rho_{\mathrm{UB}} = 1$, whilst the weights take values between $\omega_{\mathrm{LB}} = 0.5$ and $\omega_{\mathrm{UB}} = 10$. The inner components of the knot vectors are evenly distributed in the interval $]0,1[$. The post-processing operations are performed in ParaView® and ANSYS® environments.

The main purpose of the analyses presented in the following subsections is to validate the proposed framework when dealing with thermomechanical TO problems through a comparison with the results available in the literature. Furthermore, several sensitivity analyses are performed to investigate the following aspects:

1. The influence of different penalisation schemes and their parameters on the optimised topologies;
2. The influence of the entity used to describe the pseudo-density field, i.e., B-spline or NURBS (only for 2D problems for the sake of brevity);
3. The influence of the number of CPs and degrees of Bernstein's polynomial on the optimised solution (only for 2D problems for the sake of brevity);
4. The combined effect of inhomogeneous Neumann-Dirichlet BCs and thermomechanical DDLs on the optimised topology (only for 2D problems for the sake of brevity);
5. The effect of a design-dependent heat sources on the optimised topologies (only for 2D problems for the sake of brevity).

4.1. 2D benchmark structures

The first benchmark problem (BP), taken from [32] and shown in Fig. 1, deals with the Messerschmitt Bölkow Blohm beam submitted to thermomechanical loads.

The geometrical parameters defining the first 2D BP (BP1-2D) are: $L_1 = 1200$ mm, $L_2 = 400$ mm and $t = 10$ mm (thickness of the plate). The FE model is constituted of $N_e = 120 \times 40$ plane elements with four nodes with two mechanical DOFs and one thermal DOF per node and plane stress hypothesis [52]. This element type is used for all the 2D BPs illustrated in this section. The FE model is subjected to the following BCs:

- $u_1 = 0$ is set on the nodes located at $x_1 = 0$;
- $u_2 = 0$ is set on the node located at $(x_1, x_2) = (L_1, 0)$;
- A concentrated load of magnitude $F_m = 10$ kN is applied on the node $(x_1, x_2) = (0, L_2)$;
- A temperature $\theta_{\mathrm{cold}} = 273.15$ K is imposed on the nodes located at $x_2 = L_2$;
- A temperature $\theta_{\mathrm{hot}} = 1073.15$ K is imposed on the nodes located at $x_2 = 0$;
- $\theta_{\mathrm{ref}} = 273.15$ K is considered as reference temperature for the calculation of the thermal strain vector, whilst adiabatic condition is imposed on the rest of the boundary.

The material properties used for BP1-2D are: $E = 30$ GPa (Young's modulus), $\nu = 0.3$ (Poisson's coefficient), $\varrho = 1$ Kg.mm^{-3}, $k = 1$ W.(mK)$^{-1}$ (thermal conductivity) and $\chi = 12 \times 10^{-6}$ K^{-1} (coefficient of thermal expansion).

The second 2D BP (BP2-2D), shown in Fig. 2, has been deeply investigated in [23,45,53]. Its geometrical parameters are: $L_1 = 720$ mm, $L_2 = 477$ mm and $t = 10$ mm (thickness of the plate). The FE model is constituted of $N_e = 100 \times 80$ plane elements and is subjected to the following BCs:

- The nodes located at $x_1 = 0$ and $x_1 = L_1$ are clamped;
- A concentrated load of magnitude $F = 10$ kN is applied on the node $(x_1, x_2) = (\frac{L_1}{2}, 0)$;
- A temperature $\theta_{\mathrm{ref}} = 293.15$ K is imposed on the nodes located at $x_1 = 0$ and $x_1 = L_1$;
- A constant heat source of magnitude $P = \{0; 0.5; 1\}$ W is applied on the node located at $(x_1, x_2) = (\frac{L_1}{2}, 0)$;
- $\theta_{\mathrm{ref}} = 293.15$ K is considered as reference temperature for the calculation of the thermal strain vector, whilst adiabatic condition is imposed on the rest of the boundary.

The material properties used for BP2-2D are: $E = 210$ GPa (Young's modulus), $\nu = 0.27$ (Poisson's coefficient), $\varrho = 7.8 \times 109^{-6}$ Kg.mm^{-3}, $k = 80 \times 10^{-3}$ W.(mK)$^{-1}$ (thermal conductivity) and $\chi = 11 \times 10^{-6}$ K^{-1} (coefficient of thermal expansion).

The third 2D BP (BP3-2D), shown in Fig. 3, is characterised by the same geometrical parameters and the same mesh as BP2-2D. For this benchmark problem, the following BCs have been considered:

- $u_1 = u_2 = 0$ is imposed on the node located at $(x_1, x_2) = (0, 0)$;
- $u_2 = 0$ is imposed on the node located at $(x_1, x_2) = (L_1, 0)$;
- Regarding the inhomogeneous BC of the Dirichlet's type either $u_1 = \delta_1$ is imposed on the node located at $(x_1, x_2) = (L_1, 0)$ or $u_1 = \delta_2$ is imposed on the node located at $(x_1, x_2) = (L_1, L_2)$;

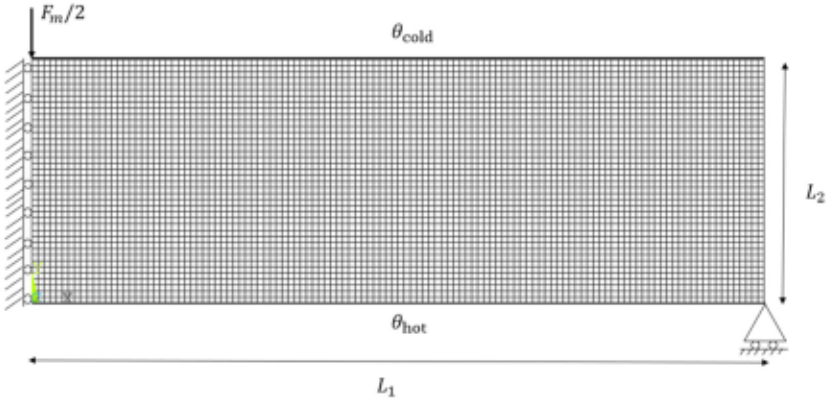

Fig. 1. Geometry, mesh and boundary conditions of BP1-2D.

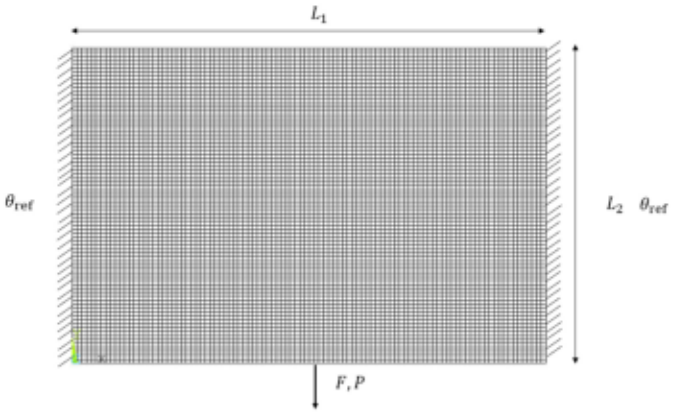

Fig. 2. Geometry, mesh and boundary conditions of BP2-2D.

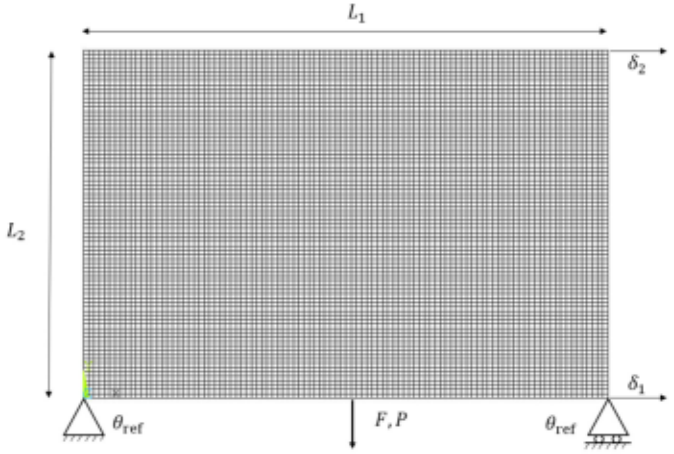

Fig. 3. Geometry, mesh and boundary conditions of BP3-2D.

- A point force $F = 10$ kN is applied on the node $(x_1, x_2) = \left(\frac{L_1}{2}, 0\right)$;
- A constant heat source of magnitude $P = 1$ W is applied on the node located at $(x_1, x_2) = \left(\frac{L_1}{2}, 0\right)$
- A temperature $\theta_{ref} = 293.15$ K is applied on the nodes located at $(x_1, x_2) = (0, 0)$ and $(x_1, x_2) = (L_1, 0)$;
- Adiabatic condition is imposed on the rest of the boundary

The imposed displacement δ_1 and δ_2 take the following values $\delta_1 = \delta_2 = \{-7, -3.5, 0, 3.5, 7\} \times 10^{-3}$ mm. The same material as BP2-2D is considered.

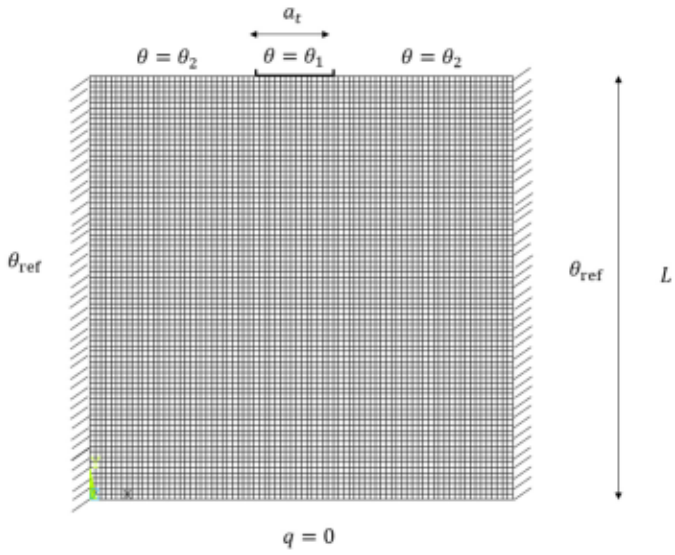

Fig. 4. Geometry, mesh and boundary conditions of BP4-2D.

The last 2D benchmark (BP4-2D), shown in Fig. 4, is characterised by the presence of design-dependent heat sources distributed over the domain, which to the best of the authors' knowledge has never been studied up to now when considering thermomechanical TO problems. The geometrical parameters defining BP4-2D are: $L = 20$ mm (the design domain is a square), $a_t = 2$ mm and $t = 1$ mm (thickness of the plate). The FE model is constituted of $N_e = 80 \times 80$ plane elements and is subjected to the following BCs:

- The nodes located at $x_1 = 0$ and $x_1 = L$ are clamped;
- Adiabatic condition is imposed on the nodes located at $x_2 = 0$;
- A temperature $\theta_{ref} = 293.15$ K is imposed on the nodes located at $x_1 = 0$ and $x_1 = L$;
- A temperature $\theta = \theta_1$ is imposed on the nodes located at $x_1 \in \left[\frac{L-a_t}{2}, \frac{L-a_t}{2}\right]$, $x_2 = L$.
- A temperature $\theta = \theta_2$ is imposed on the nodes located at $x_1 \in \left[0, \frac{L-a_t}{2}\right]$, $x_2 = L$ and $x_1 \in \left[\frac{L+a_t}{2}, L\right]$, $x_2 = L$;
- A heat source equal to $S_h = 0.001$ W.mm^{-3} is evenly distributed over the whole design domain;
- $\theta_{ref} = 293.15$ K is considered as reference temperature.

The material properties used for BP4-2D are: $E = 210$ GPa (Young's modulus), $\nu = 0.3$ (Poisson's coefficient), $\rho = 7.8 \times 10^{-6}$ Kg.mm^{-3}, $k = 80$ W.(mmK)$^{-1}$ (thermal conductivity) and $\chi = 11 \times 10^{-6}$ K^{-1} (coefficient of

Table 2
Design cases considered for BP1-2D.

ϕ_i	DC1	DC2	DC3	DC4	DC5	DC6
$\mathbf{f}_{\hat{\theta}}$	Eq. (38), $\alpha = 3$	Eq. (38), $\alpha = 3$	Eq. (38), $\alpha = 3$	Eq. (39), $q = 4$	Eq. (40), $\beta = 1$	Eq. (40), $\beta = 1$
$\mathbf{K}$	Eq. (38), $\alpha = 3$	Eq. (38), $\alpha = 3$	Eq. (38), $\alpha = 3$	Eq. (39), $q = 4$	Eq. (38), $\alpha = 3$	Eq. (39), $q = 4$
$\mathbf{K}_{\hat{\theta}}$	Eq. (38), $\alpha = 3$	Eq. (38), $\alpha = 1$	Eq. (38), $\alpha = 0.5$	Eq. (39), $q = 4$	Eq. (38), $\alpha = 0.5$	Eq. (39), $q = 4$

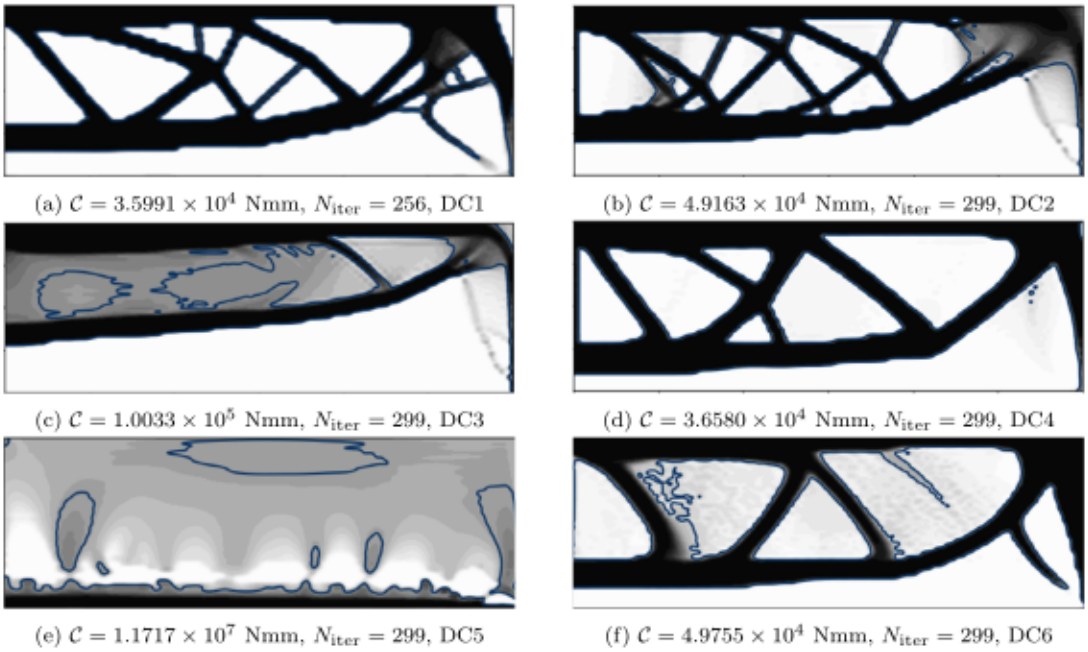

(a) $\mathcal{C} = 3.5991 \times 10^4$ Nmm, $N_{\text{iter}} = 256$, DC1
(b) $\mathcal{C} = 4.9163 \times 10^4$ Nmm, $N_{\text{iter}} = 299$, DC2
(c) $\mathcal{C} = 1.0033 \times 10^5$ Nmm, $N_{\text{iter}} = 299$, DC3
(d) $\mathcal{C} = 3.6580 \times 10^4$ Nmm, $N_{\text{iter}} = 299$, DC4
(e) $\mathcal{C} = 1.1717 \times 10^7$ Nmm, $N_{\text{iter}} = 299$, DC5
(f) $\mathcal{C} = 4.9755 \times 10^4$ Nmm, $N_{\text{iter}} = 299$, DC6

Fig. 5. BP1-2D: influence of the penalisation scheme on the optimised topology considering the DCs in Table 2.

thermal expansion). The imposed temperatures θ_1 and θ_2 take the following values: $\theta_i = \{273.15; 146.575; 293.15\}$ K $(i = 1, 2)$.

4.1.1. BP1-2D: sensitivity of the optimised topology to the penalisation schemes

The goal of this first set of analyses conducted on BP1-2D is to study the influence of the penalisation schemes used for the element stiffness matrix, element thermal conductivity matrix and the element thermo-mechanical DDLs in structural analysis on the optimised topology. The numerical simulations are carried out considering a NURBS surface as a descriptor of the pseudo-density field with degrees $p_1 = p_2 = 3$. The number of CPs is equal to $N_{\text{CP}} = 100 \times 60$. A volume fraction equal to $\gamma = 0.4$ and the design cases (DCs) listed in Table 2 are considered in this campaign of analyses. The initial solution is characterised by a uniform pseudo-density field fulfilling the constraint on the volume fraction. The CNLPP of Eq. (37) has been solved by considering a maximum number of iterations equal to $N_{\text{iter}}^{\max} = 300$.

The optimal topologies obtained with the proposed approach, for each design case, are shown in Fig. 5 in terms of compliance and number of iterations N_{iter} to achieve convergence. The optimised solution available in the literature for the same benchmark problem presented in [32] is illustrated in Fig. 6.

From the analysis of the results shown in Figs. 5 and 6, the following remarks can be drawn.

Firstly, when comparing the results obtained with the NURBS-density-based method and those presented in [32], the former converge better through black and white topologies for DCs 1 and 4 than the latter: a quick glance to Figs. 5a, 5d and 6 suffices to understand this fact. Moreover, the optimised topology presented in [32], which has been found using the classic density-based TO algorithm, has been determined by considering the penalty schemes corresponding to DC1 in Table 2. By comparing the solution found using the NURBS-density-based method

Fig. 6. BP1-2D: optimised topology taken from [32]; $\mathcal{C} = \text{N.A.}$, $N_{\text{iter}} = 299$, DC1.

for DC1 with that taken from [32] and shown in Fig. 6, two important differences can be observed. On the one hand, the solution shown in Fig. 5a converges towards a well-defined truss-like configuration in 256 iterations with intermediate values of the pseudo-density field occurring only in the region on the bottom-right of the figure. This corresponds to the formation of an oblique thin strut, which is due to the localised support BCs. On the other hand, the solution found in [32] presents a wide region characterised by intermediate values of the pseudo-density field and the final topology, which has been found after 299 iterations, does not correspond to a truss-like configuration. These differences are mainly related to: a) the filtering strategy (which is not needed when using a topological descriptor based on a NURBS entity), b) the gradient calculation (which exploits the properties of the local support property of the NURBS basis functions in our case) and c) the algorithm used to carry out the solution search of problem (37), i.e., GCMMA in our case vs. method of moving asymptotes in [32]. Unfortunately, the compliance of the optimised solution shown in Fig. 6 is not provided in [32]; accordingly, a quantitative comparison between our results and that found in [32] in terms of mechanical performances is not possible.

Secondly, regarding the first three DCs where the SIMP penalisation scheme is used with different values of α, decreasing the value of α when penalising the thermal conductivity matrix leads to convergence issues.

Table 3
Design cases considered for BP2-2D.

ϕ_i	DC1	DC2	DC3	DC4	DC5	DC6	DC7
$\mathbf{f}_\phi$	Eq. (39), $q=4$				Eq. (38), $\alpha=3$		
$\mathbf{K}$	Eq. (39), $q=8$		Eq. (39), $q=4$		Eq. (38), $\alpha=3$		
$\mathbf{K}_\phi$	Eq. (39), $q=4$	Eq. (39), $q=8$	Eq. (39), $q=4$	Eq. (39), $q=8$	Eq. (38), $\alpha=3$	Eq. (38), $\alpha=1$	Eq. (38), $\alpha=0.5$

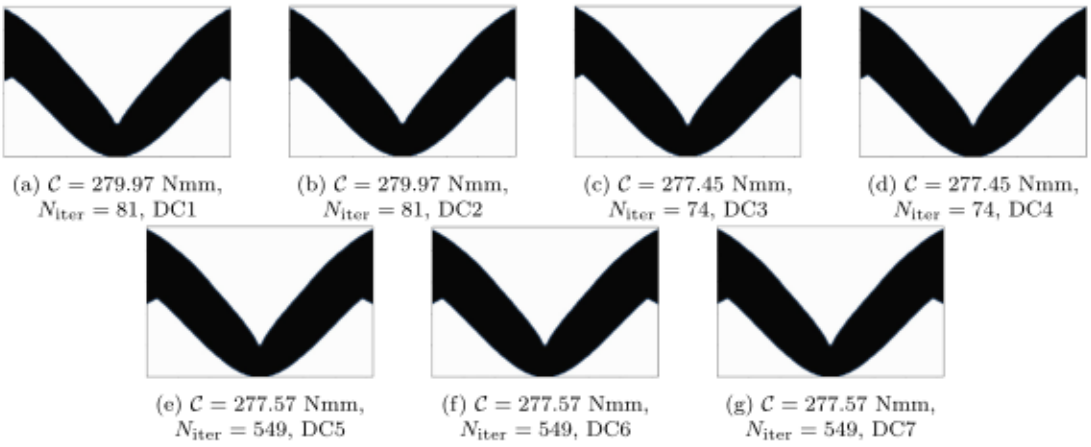

(a) $\mathcal{C} = 279.97$ Nmm, $N_{\text{iter}} = 81$, DC1
(b) $\mathcal{C} = 279.97$ Nmm, $N_{\text{iter}} = 81$, DC2
(c) $\mathcal{C} = 277.45$ Nmm, $N_{\text{iter}} = 74$, DC3
(d) $\mathcal{C} = 277.45$ Nmm, $N_{\text{iter}} = 74$, DC4
(e) $\mathcal{C} = 277.57$ Nmm, $N_{\text{iter}} = 549$, DC5
(f) $\mathcal{C} = 277.57$ Nmm, $N_{\text{iter}} = 549$, DC6
(g) $\mathcal{C} = 277.57$ Nmm, $N_{\text{iter}} = 549$, DC7

Fig. 7. BP2-2D solutions with $P = 0$ W when considering the DCs in Table 3.

This is related to the implicit penalisation of the thermal strain deriving from the solution of the thermal equilibrium problem.

Thirdly, when comparing the solutions obtained with SIMP and RAMP schemes, i.e., DCs 1-4 in Table 2, although the final compliance and number of iterations are comparable, the optimised topologies are substantially different and a clear black and white design can be obtained only when using the RAMP scheme (DC4). This result is due to the better behaviour of the RAMP scheme when the element pseudo-density goes to zero.

Finally, the use of the modified linear penalisation scheme for DDL does not allow obtaining clear black and white designs when considering thermomechanical analyses, unlike the case of inertial loads where it allows to find the best solutions [50]. This discrepancy can be explained by examining the dependence of the design-dependent forces of Eqs. (20) and (21) on the pseudo-density field. In the case of inertial loads, this dependence is solely explicit, whereas in the context of thermomechanical analyses, the vector of design-dependent forces is implicitly dependent on the pseudo-density field through the temperature field. Accordingly, linear penalisation scheme does not represent a good choice in this case.

4.1.2. BP2-2D: sensitivity of the optimised topology to the penalisation schemes parameters

The focus of the first campaign of analyses conducted on BP2-2D is the study of the influence of the SIMP and RAMP schemes parameters on the optimised solution. The numerical simulations are carried out considering a NURBS surface as a descriptor of the pseudo-density field with degrees $p_1 = p_2 = 3$. The number of CPs is equal to $N_{\text{CP}} = 90 \times 60$. The imposed volume fraction is $\gamma = 0.4$ and the initial guess is a uniform pseudo-density field satisfying the constraint on the volume fraction. The DCs considered for this first campaign of analyses are listed in Table 3. For each DC, the optimisation process is performed by considering three values of the applied thermal load, i.e., $P = 0,\ 0.5,\ 1$ W. The maximum number of iterations is set as $N_{\text{iter}}^{\max} = 550$.

The optimised topologies obtained for the multiple DCs are illustrated in Figs. 7, 8 and 9 for $P = 0$ W, $P = 0.5$ W and $P = 1.0$ W, respectively.

The following remarks can be inferred from the analysis of these results. Firstly, as expected, regardless of the considered penalisation schemes, the higher P, the higher the cost function value. Secondly, when the RAMP scheme is used for the stiffness matrix, thermal conductivity matrix and design-dependent forces, i.e., DCs 1-4, the best results, in terms of generalised compliance value and number of iterations, are achieved for DC3, i.e., when $q = 4$ for all the penalisation schemes. Moreover, regardless of the value of the applied thermal load P and of the parameter q used in Eq. (39), the final topology is almost the same (except the case $P = 1$ where two small holes appear on the left and right regions of the domain when considering DC3). Thirdly, regarding the use of the SIMP scheme, i.e., DCs 5-7, the best results in terms of generalised compliance are achieved for DC7. Moreover, the greater P, the more significant the differences between the optimised topologies for the considered DCs. However, a convergence towards a clear black and white design is achieved only for DC5 when $P = 1$ W. It is noteworthy that when comparing the solutions obtained with RAMP and SIMP schemes, lower values of the compliance are obtained when considering the SIMP scheme, although the RAMP scheme allows reaching the convergence in approximately the half of iterations.

Finally, to better understand and compare the results shown in Figs. 8 and 9 a cross-check analysis has been performed. The idea is to take the optimised pseudo-density field obtained in a given DC and to evaluate its performance, in terms of the generalised compliance, by considering the penalisation schemes used in the other DCs. Of course, since the solutions found in the case $P = 0$ W are almost identical, the cross-check analysis is performed only for the solutions obtained in the cases $P = 0.5$ W and $P = 1$ W. The results of the cross-check analysis are reported in Tables 4 and 5 for the cases $P = 0.5$ W and $P = 1$ W, respectively.

The following remarks can be drawn from the analysis of the results reported in Tables 4 and 5. Firstly, for the case $P = 0.5$ W, the solution found when considering the penalisation schemes used for DC7 is that characterised by the lowest value of the generalised compliance when checked by using the penalisation schemes used for the other DCs. Secondly, the same remark can be done for the case $P = 1$ W, with the only exception of the solution found when considering DC6 and checked with the penalisation schemes used for DC1, which is characterised by the

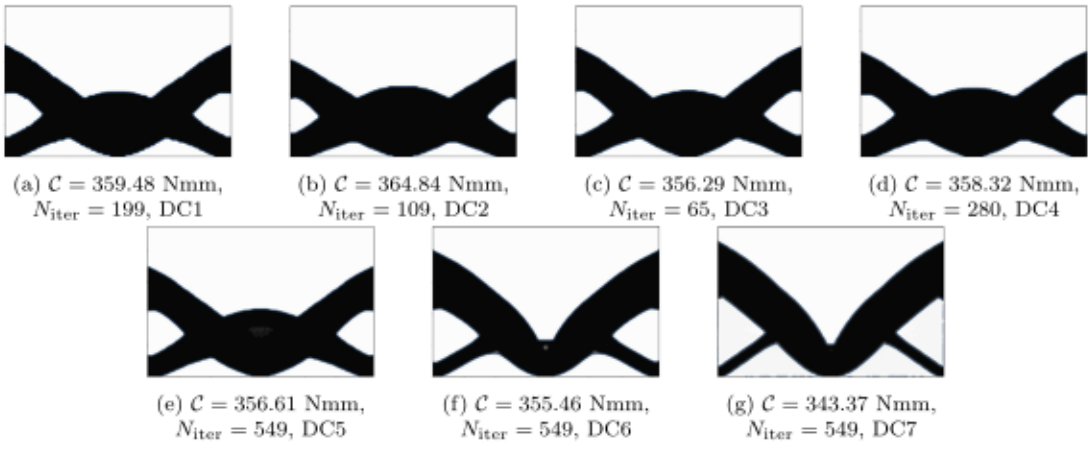

(a) $\mathcal{C} = 359.48$ Nmm, $N_{\text{iter}} = 199$, DC1
(b) $\mathcal{C} = 364.84$ Nmm, $N_{\text{iter}} = 109$, DC2
(c) $\mathcal{C} = 356.29$ Nmm, $N_{\text{iter}} = 65$, DC3
(d) $\mathcal{C} = 358.32$ Nmm, $N_{\text{iter}} = 280$, DC4
(e) $\mathcal{C} = 356.61$ Nmm, $N_{\text{iter}} = 549$, DC5
(f) $\mathcal{C} = 355.46$ Nmm, $N_{\text{iter}} = 549$, DC6
(g) $\mathcal{C} = 343.37$ Nmm, $N_{\text{iter}} = 549$, DC7

Fig. 8. BP2-2D solutions with $P = 0.5$ W when considering the DCs in Table 3.

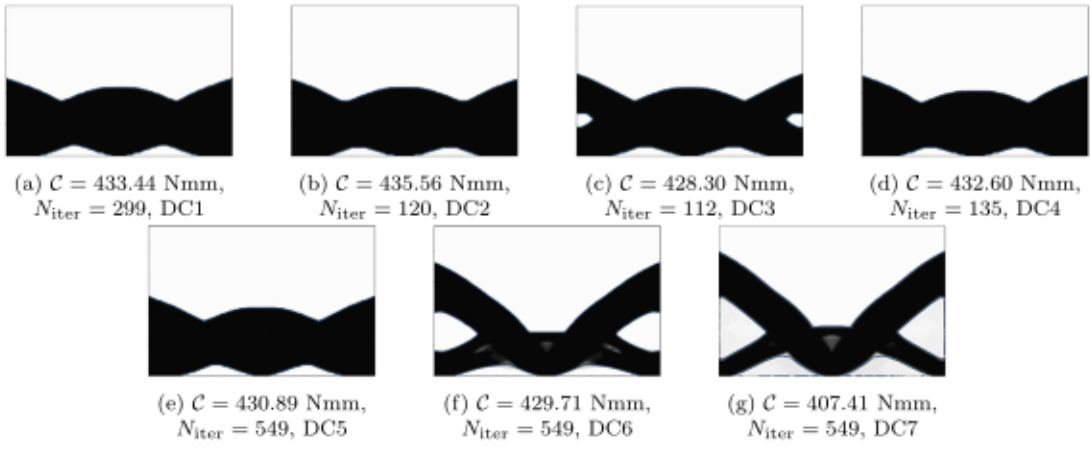

(a) $\mathcal{C} = 433.44$ Nmm, $N_{\text{iter}} = 299$, DC1
(b) $\mathcal{C} = 435.56$ Nmm, $N_{\text{iter}} = 120$, DC2
(c) $\mathcal{C} = 428.30$ Nmm, $N_{\text{iter}} = 112$, DC3
(d) $\mathcal{C} = 432.60$ Nmm, $N_{\text{iter}} = 135$, DC4
(e) $\mathcal{C} = 430.89$ Nmm, $N_{\text{iter}} = 549$, DC5
(f) $\mathcal{C} = 429.71$ Nmm, $N_{\text{iter}} = 549$, DC6
(g) $\mathcal{C} = 407.41$ Nmm, $N_{\text{iter}} = 549$, DC7

Fig. 9. BP2-2D solutions with $P = 1$ W when considering the DCs in Table 3.

Table 4
Cross-check analysis for BP2-2D; values of the generalised compliance for the case $P = 0.5$ W.

		DC used to check the solution						
		DC1	DC2	DC3	DC4	DC5	DC6	DC7
DC to be assessed	DC1	359.48	364.00	359.67	360.65	362.75	366.26	379.10
	DC2	360.61	364.84	360.80	361.61	364.32	368.73	383.07
	DC3	356.23	360.83	356.29	357.37	357.66	361.23	372.96
	DC4	357.36	361.67	357.39	358.32	359.20	363.65	376.85
	DC5	356.43	361.13	356.35	357.51	356.61	360.27	375.15
	DC6	353.48	358.83	353.51	355.01	353.64	355.46	361.48
	DC7	347.99	354.45	348.30	350.28	348.40	347.38	343.37

Table 5
Cross-check analysis for BP2-2D; values of the generalised compliance for the case $P = 1$ W.

		DC used to check the solution						
		DC1	DC2	DC3	DC4	DC5	DC6	DC7
DC to be assessed	DC1	433.44	434.49	431.74	434.65	437.46	452.07	479.10
	DC2	432.54	435.56	433.30	435.74	439.60	459.47	489.83
	DC3	429.14	431.56	428.30	431.52	431.88	443.65	468.07
	DC4	430.13	432.63	429.85	432.60	433.99	450.83	478.46
	DC5	429.69	432.19	428.53	431.96	430.89	440.93	474.40
	DC6	375.71	428.97	424.67	428.82	427.23	429.71	439.69
	DC7	420.77	421.86	417.14	422.40	420.32	417.27	407.41

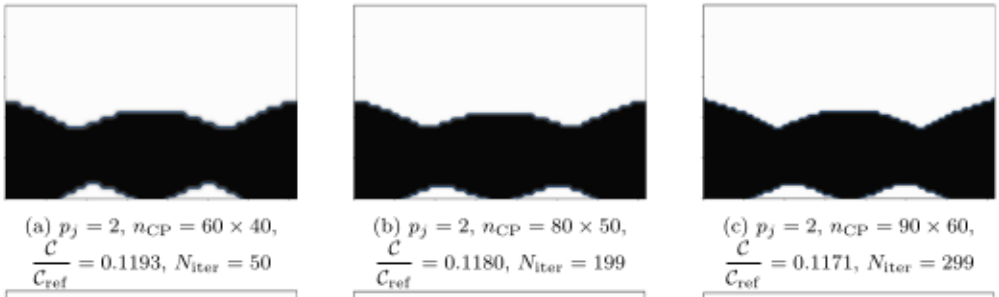

(a) $p_j = 2$, $n_{\mathrm{CP}} = 60 \times 40$, $\frac{\mathcal{C}}{\mathcal{C}_{\mathrm{ref}}} = 0.1193$, $N_{\mathrm{iter}} = 50$

(b) $p_j = 2$, $n_{\mathrm{CP}} = 80 \times 50$, $\frac{\mathcal{C}}{\mathcal{C}_{\mathrm{ref}}} = 0.1180$, $N_{\mathrm{iter}} = 199$

(c) $p_j = 2$, $n_{\mathrm{CP}} = 90 \times 60$, $\frac{\mathcal{C}}{\mathcal{C}_{\mathrm{ref}}} = 0.1171$, $N_{\mathrm{iter}} = 299$

(d) $p_j = 3$, $n_{\mathrm{CP}} = 60 \times 40$, $\frac{\mathcal{C}}{\mathcal{C}_{\mathrm{ref}}} = 0.1205$, $N_{\mathrm{iter}} = 44$

(e) $p_j = 3$, $n_{\mathrm{CP}} = 80 \times 50$, $\frac{\mathcal{C}}{\mathcal{C}_{\mathrm{ref}}} = 0.1189$, $N_{\mathrm{iter}} = 199$

(f) $p_j = 3$, $n_{\mathrm{CP}} = 90 \times 60$, $\frac{\mathcal{C}}{\mathcal{C}_{\mathrm{ref}}} = 0.1180$, $N_{\mathrm{iter}} = 199$

Fig. 10. BP2-2D: optimised topologies and objective function values for B-spline entities.

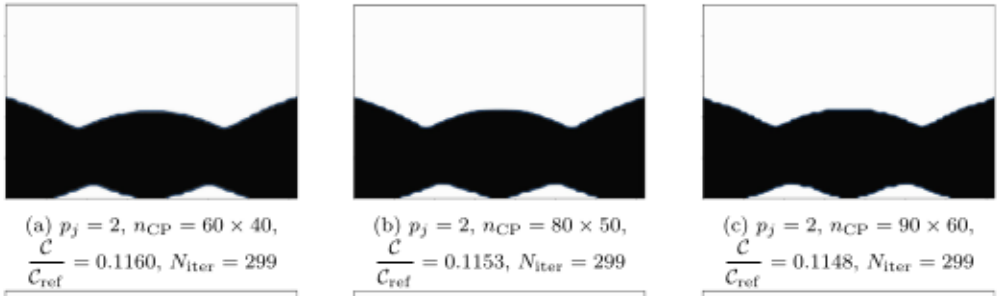

(a) $p_j = 2$, $n_{\mathrm{CP}} = 60 \times 40$, $\frac{\mathcal{C}}{\mathcal{C}_{\mathrm{ref}}} = 0.1160$, $N_{\mathrm{iter}} = 299$

(b) $p_j = 2$, $n_{\mathrm{CP}} = 80 \times 50$, $\frac{\mathcal{C}}{\mathcal{C}_{\mathrm{ref}}} = 0.1153$, $N_{\mathrm{iter}} = 299$

(c) $p_j = 2$, $n_{\mathrm{CP}} = 90 \times 60$, $\frac{\mathcal{C}}{\mathcal{C}_{\mathrm{ref}}} = 0.1148$, $N_{\mathrm{iter}} = 299$

(d) $p_j = 3$, $n_{\mathrm{CP}} = 60 \times 40$, $\frac{\mathcal{C}}{\mathcal{C}_{\mathrm{ref}}} = 0.1166$, $N_{\mathrm{iter}} = 299$

(e) $p_j = 3$, $n_{\mathrm{CP}} = 80 \times 50$, $\frac{\mathcal{C}}{\mathcal{C}_{\mathrm{ref}}} = 0.1158$, $N_{\mathrm{iter}} = 299$

(f) $p_j = 3$, $n_{\mathrm{CP}} = 90 \times 60$, $\frac{\mathcal{C}}{\mathcal{C}_{\mathrm{ref}}} = 0.1153$, $N_{\mathrm{iter}} = 299$

Fig. 11. BP2-2D: optimised topologies and objective function values for NURBS entities.

lowest compliance. This can be explained by the fact that the penalty schemes used for DC6 and DC7 allow the identification of local feasible minima characterised by a lower cost function that cannot be accessed when considering the penalty schemes used in the other DCs. Nevertheless, such solutions are still characterised by the presence of some intermediate values of the pseudo density field, see Fig. 9 for instance. Furthermore, by looking at the results reported in Tables 4 and 5, the compliance of the optimised solutions found in DCs 1-4, which are characterised by the use of the RAMP penalty scheme with different values of the parameter q, increases when checked with the SIMP penalisation scheme used in DCs5-7. The converse is not necessarily true (see for instance the compliance of the optimised topologies found for the case $P = 1$ W when considering DCs5 and DCs6 and checked with DC1). This means that the optimised topologies found by using the RAMP penalty scheme tend always to underestimate the compliance when compared to those found by considering the DCs employing the SIMP penalty scheme, at least for this benchmark problem.

4.1.3. BP2-2D: sensitivity of the optimised topology to the integer parameters of the topological descriptor

The goal of the second campaign of numerical analyses carried out on BP2-2D is to study the influence of the integer parameters of the B-spline/NURBS entity on the optimised topology. To this purpose, the following values of the number of CPs and basis functions degrees have been considered: $n_{\mathrm{CP}} = 60\times40, 80\times50, 90\times60$ and $p_1 = p_2 = 2,\ 3$. A volume fraction $\gamma = 0.4$ is used in the analyses presented in this section and the initial guess has been chosen in the same way as in the above subsections. Regarding the penalisation schemes, the DC1 reported in Table 3 and a thermal load $P = 1$ W have been considered. The maximum number of iterations for the GCMMA algorithm has been set as $N_{\mathrm{iter}}^{\mathrm{max}} = 300$. The optimised topologies are reported in Figs. 10 and 11 for B-spline and NURBS solutions, respectively. In the same figures, the dimensionless compliance and number of iterations N_{iter} to achieve convergence for each solution are also reported. Fig. 12 shows the trend of the dimensionless objective function vs. the number of CPs for the different degrees for both B-spline and NURBS solutions. As expected, in line with

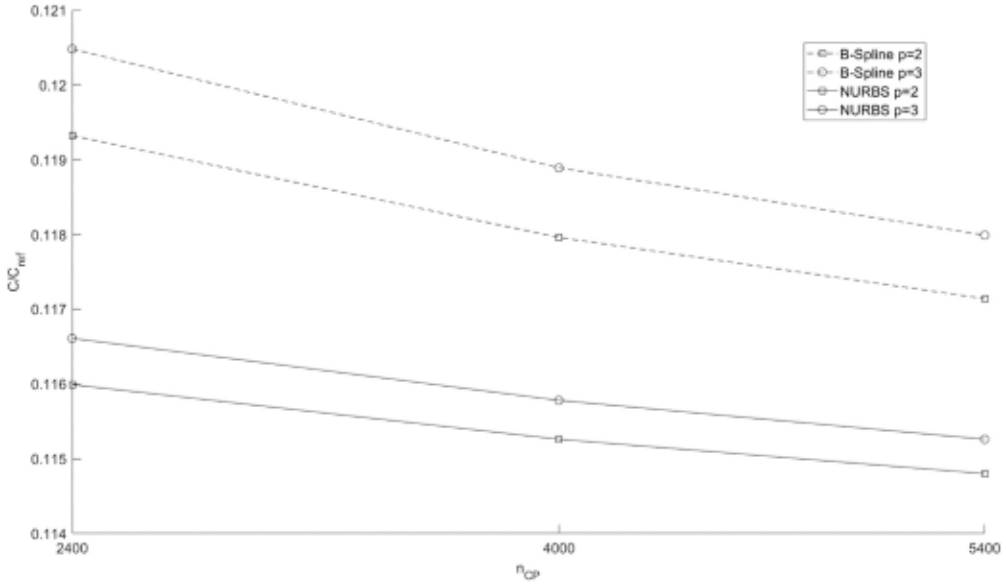

Fig. 12. BP2-2D: objective function vs. number of control points for different degrees of the basis functions.

the results obtained for standard TO problems with design-independent loads [46], the lower the degree and/or the higher the CPs number, the lower the cost function value. As explained in [46], this result is due to the local support property of the NURBS basis functions. Moreover, compared to their B-spline counterparts, NURBS solutions have a lower cost function and smoother boundaries, regardless of the number of CPs and the degrees of the Bernstein's polynomials.

4.1.4. BP3-2D: sensitivity of the optimised topology to mixed non-zero boundary conditions

The aim of the numerical analyses conducted on BP3-2D is to evaluate the combined effect of thermomechanical DDLs and inhomogeneous Dirichlet boundary conditions. The numerical simulations are carried out considering a NURBS surface as a descriptor of the pseudo-density field with degrees $p_1 = p_2 = 3$. The number of CPs is equal to $N_{\text{CP}} = 90 \times 60$. The analyses presented in this section are carried out considering both the RAMP and SIMP schemes characterised by the parameters of DC3 and DC5, respectively, as reported in Table 3. The imposed volume fraction is $\gamma = 0.4$ and a feasible uniform pseudo-density field is taken as initial guess. The CNLPP of Eq. (37) is solved by setting $N_{\text{iter}}^{\max} = 300$ as maximum number of iterations. Two scenarios are considered: in the first one only the displacement δ_2 in Fig. 3 is applied by considering the following values $\delta_2 = \{-7, -3.5, 0, 3.5, 7\} \times 10^{-3}$ mm, whereas in the second one only the displacement δ_1 in Fig. 3 is applied by considering the following values $\delta_1 = \{-7, -3.5, 0, 3.5, 7\} \times 10^{-3}$ mm. The optimised solutions are shown in Figs. 13-16 in terms of generalised compliance vs. the applied displacement. For each optimised topology, the number of iterations to achieve convergence is also given in each plot.

From the analysis of the results, the following remarks can be drawn. Firstly, as illustrated in Figs. 13 and 14, the same trend of the generalised compliance vs. the imposed displacement is found when δ_1 is applied to the structure. The penalisation scheme has a weak influence on the optimised topology when varying the displacement δ_1. Specifically, the most significant differences between optimised topologies, obtained when considering DC3 and DC5 in Table 3, can be observed only for positive values of δ_1: the solutions obtained with the SIMP scheme are characterised by a higher number of holes and one of them is not symmetric. Moreover, the generalised compliance takes negative values for $\delta_1 = -7 \times 10^{-3}$ mm and becomes positive increasing the applied displacement. Nevertheless, when the displacement is applied on the top of the structure (δ_2), the trend of the generalised compliance vs. the applied displacement is strongly affected by the penalisation scheme used in the analysis. When the RAMP scheme is considered (DC3 in Table 3), the trend is not monotone, as show in Fig. 15. Conversely, when the SIMP scheme is used, (DC5 in Table 3) the trend is monotone. Specifically, for $\delta_2 = -7 \times 10^{-3}$ mm, when using the RAMP scheme, the GCMMA algorithm is able to find a feasible minimiser characterised by a generalised compliance lower than that of the solution found when using the SIMP scheme. Moreover, it is noteworthy that, regardless of the considered DC, the generalised compliance takes negative value only when $\delta_2 = 7 \times 10^{-3}$ mm. Finally, unlike the BPs discussed above, in this case, the solutions obtained with the RAMP scheme outperform those obtained with the SIMP scheme (in terms of generalised compliance) regardless of the value of the applied displacement.

Table 6
Design cases considered for BP4-2D.

DC1	DC2	DC3
$\theta_1 = 0, \theta_2 = \theta_{\text{ref}}$	$\theta_1 = \theta_2 = \theta_{\text{ref}}$	$\theta_1 = 0, \theta_2 = \theta_{\text{ref}}/2$

4.1.5. BP4-2D: influence of design-dependent heat sources on the optimised topology

The aim of the numerical analyses performed on BP4-2D is to study the effect of a design-dependent heat source distributed within the domain on the optimised solution. The pseudo-density field is described by a NURBS surface characterised by $n_{\text{CP}} = 68 \times 68$ CPs and degrees of the Bernstein's polynomials equal to $p_1 = p_2 = 2$. A volume fraction equal to $\gamma = 0.4$ is considered and $N_{\text{iter}}^{\max} = 500$ has been taken as maximum number of iteration for the resolution of Eq. (37). As for the other benchmark problems, the initial guess is an uniform pseudo-density field satisfying the constraint on the volume fraction. Regarding the imposed temperatures θ_1 and θ_2 in Fig. 4, three DCs are considered, which are listed in Table 6. For all DCs, the RAMP scheme with $q = 4$ is used to penalise the stiffness and thermal conductive matrices as well as the vector of design-dependent thermal forces. Conversely, the distributed heat source ψ_{DD} of Eq. (14) is penalised using the modified linear scheme in Eq. (40) with $\beta = 1$.

The results are shown in Fig. 17 wherein the optimal designs are reported for each DC in terms of generalised compliance and number of iterations N_{iter} to achieve convergence. When $\theta_1 = \theta_2 = \theta_{\text{ref}}$, the thermal strains are null, thus the material is put in the region located near the top wall (Fig. 17) where such BCs are imposed. For DC1 one can

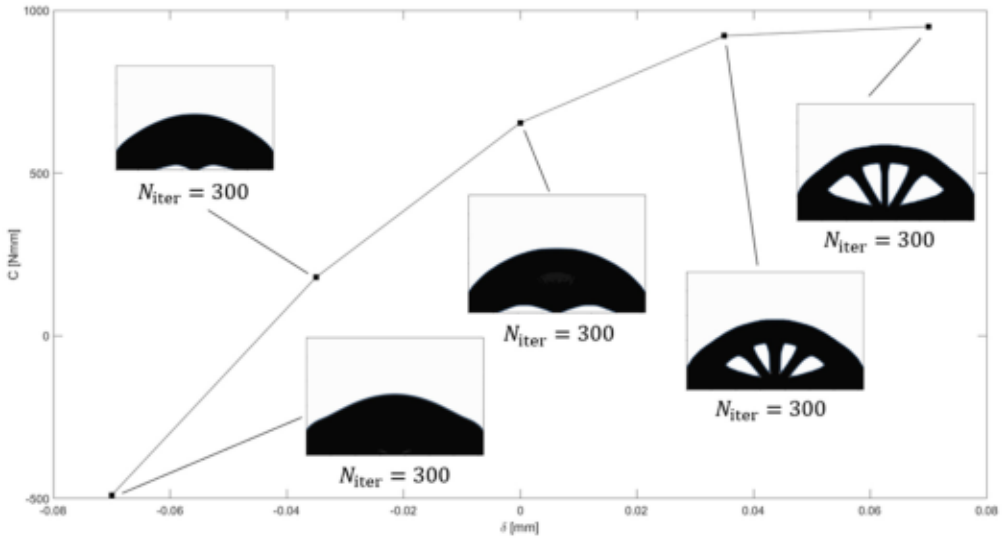

Fig. 13. BP3-2D, DC3 in Table 3: generalised compliance vs. applied displacement δ_1.

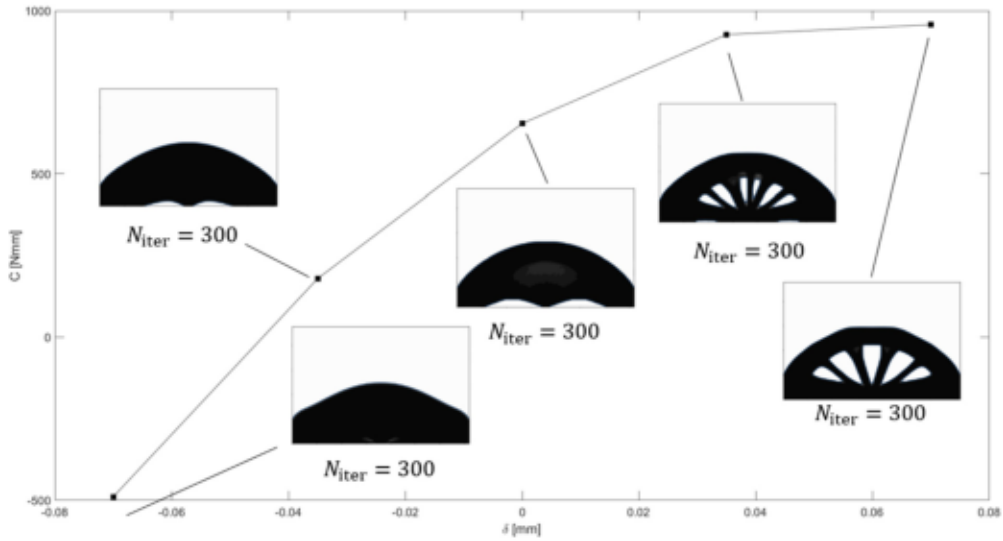

Fig. 14. BP3-2D, DC5 in Table 3: generalised compliance vs. applied displacement δ_1.

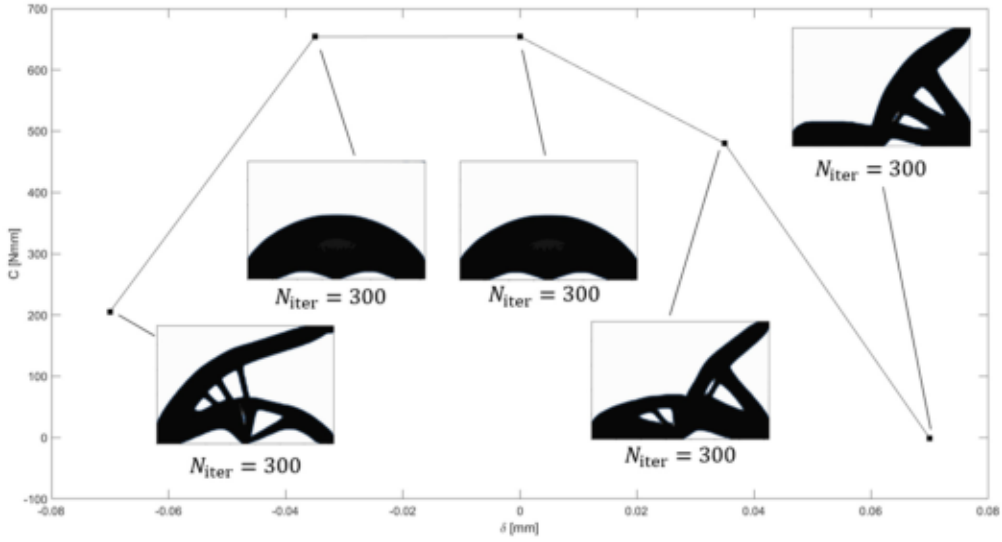

Fig. 15. BP3-2D, DC3 in Table 3: generalised compliance vs. applied displacement δ_2.

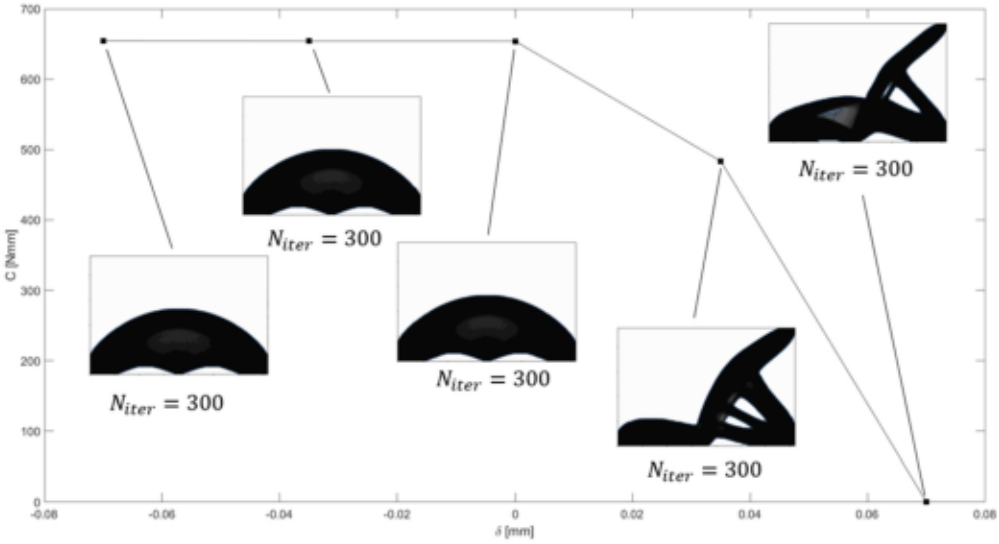

Fig. 16. BP3-2D, DC5 in Table 3: generalised compliance vs. applied displacement δ_2.

(a) $\mathcal{C} = 9.2913 \times 10^{-6}$ Nmm, $N_{\text{iter}} = 499$ (b) $\mathcal{C} = 7.7989 \times 10^{-6}$ Nmm, $N_{\text{iter}} = 499$ (c) $\mathcal{C} = 1.8588 \times 10^{-5}$ Nmm, $N_{\text{iter}} = 333$

Fig. 17. BP4-2D: influence of the boundary conditions and of a design-dependent distributed heat source on the optimised topology.

see that the pseudo-density of the elements located near the region of the top wall where $\theta_1 = 0$ is imposed, converges towards ρ_{LB}, while for DC3, a "void strip" occurs near the top wall due to the imposed BCs, which involve non-null thermal strains. In this case the convergence is apparently reached in less iterations compared to the other two DCs, but looking at the optimised design, it becomes clear that the topology does not converge through a clear black and white solution, suggesting that a local minimum has been reached. Finally, the mechanical interpretation of the optimised solutions illustrated in Fig. 17 is quite immediate: to minimise the compliance, the optimiser put the material in the regions wherein the thermal strain tends to zero by minimising, simultaneously, the intensity of the design-dependent distributed thermal source and by fulfilling the equality constraint on the volume fraction.

4.2. 3D benchmark structure

The geometry and the FE model of the 3D benchmark problem (BP-3D) are shown in Fig. 18. The geometry of the design domain is a parallelepiped with size $L_1 = 720$ mm, $L_2 = 50$ mm and $L_3 = 477$ mm. The material properties used in this case are the same used for BP2-2D. The FE model is subjected to the following BCs:

- The nodes located at $\left[x_1 = 0,\ x_2 \in (0, L_2),\ x_3 \in \left(\frac{L_3}{2} - 3e_{\text{size}}, \frac{L_3}{2} + 3e_{\text{size}}\right)\right]$, with $e_{\text{size}} = 9$ mm, are clamped and $\theta = \theta_{\text{ref}}$ is imposed;
- On the node located at $(x_1, x_2, x_3) = (L_1/2, L_2/2, 0)$ both a concentrated load $F = 10$ kN and a heat source $P = 1$ W are applied;

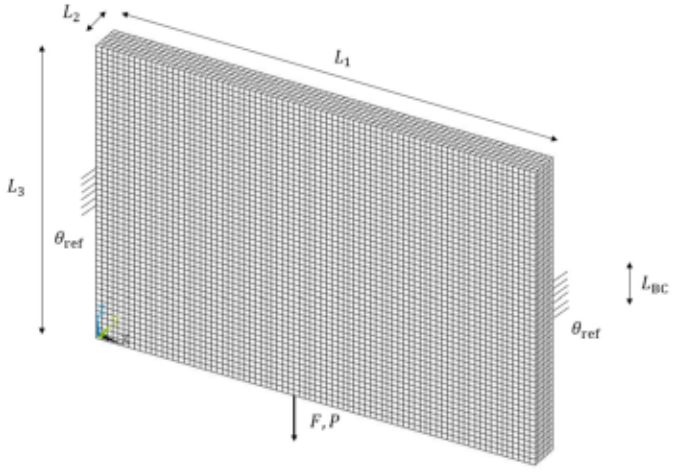

Fig. 18. Geometry, finite element model and boundary conditions of the 3D benchmark structure.

- $\theta_{\text{ref}} = 293.15$ K is considered as reference temperature and adiabatic wall condition is imposed on the rest of the boundary.

A mesh constituted of $N_e = 80 \times 6 \times 53$ solid elements with eight nodes with three structural DOFs and one thermal DOF per node is used [52].

(a) DC3 in Table 3: $\mathcal{C} = 6.34 \times 10^3$ Nmm, $N_{\text{iter}} = 799$.

(b) DC5 in Table 3: $\mathcal{C} = 6.34 \times 10^3$ Nmm, $N_{\text{iter}} = 799$.

Fig. 19. BP-3D: influence of the penalisation scheme on the optimised topology.

4.2.1. BP-3D: influence of the penalisation scheme on the optimised topology

The results presented in this section aims to illustrate the effectiveness of the proposed approach when dealing with a 3D benchmark problem. The analyses are conducted considering a volume fraction $\gamma = 0.4$ and DCs 3 and 5 in Table 3. As in the case of 2D TO problems, an uniform pseudo-density field satisfying the equality constraint on the volume fraction is considered as initial guess. The CNLPP of Eq. (37) has been solved by considering a maximum number of iterations equal to $N_{\text{iter}}^{\max} = 800$. The numerical simulations are performed considering NURBS entities with degrees $p_1 = p_2 = p_3 = 3$ and a control net constituted of $65 \times 5 \times 45$ CPs. The results are shown in Fig. 19.

It is noteworthy that both RAMP (DC3) and SIMP (DC5) schemes lead to comparable values of generalised compliance, although the optimised topologies are not exactly the same; in fact, the thickness variation occurring in the centre of the domain affects a region of different size for the two optimised solutions. Specifically, the thickness is reduced in the region situated at the centre of the design domain on the elements located on the outer boundary, i.e., at $x_2 = \pm\frac{L_2}{2}$, because a significant proportion of the heat flux is confined to the plane $x_1 - x_3$. Accordingly, the elements situated far from this plane do not contribute to the gradient of the temperature and, consequently, do not contribute to the thermal strains (hence to the generalised compliance). Finally, the same comments already made for the 2D BPs also apply to this case.

5. Conclusions

In this paper, thermomechanical TO problems have been formulated and solved in the framework of the NURBS-density-based TO algorithm. Four main contributions can be identified.

Firstly, the influence of different penalty schemes on the optimised topology is investigated by considering different combinations of penalty functions. When considering thermomechanical problems, better designs are achieved by using RAMP and SIMP schemes. Consequently, a second investigation has been carried out for these penalisation schemes to determine the most efficient set of parameters. Numerical results obtained on 2D benchmarks problems allow concluding that the best compromise in terms of cost function value and quality of the optimised topology can be obtained when using the RAMP scheme with $q = 4$ or the SIMP scheme with $\alpha = 3$ for the stiffness matrix, the thermal conductivity matrix and the thermal load without major differences.

Secondly, a sensitivity analysis of the optimised solution to the integer parameters involved in the definition of the NURBS entity has been performed, highlighting that the higher the number of CPs (or the lower the degree of Bernstein polynomials), the lower the objective function. Furthermore, NURBS solutions have a lower cost function and smoother boundaries than B-spline solutions. These results are in agreement with the trend observed for standard TO problems under design-independent loads.

Thirdly, the combined effect of thermomechanical DDLs and inhomogeneous Dirichlet boundary conditions is studied for the first time, bringing out that coherent results are obtained for RAMP and SIMP schemes and that the former scheme allows finding optimised solutions outperforming those found with the latter scheme.

Fourthly, the influence of a design-dependent distributed heat source on the optimal solution has been investigated. The presence of a design-dependent heat source distributed over the domain increases the problem complexity. However, the algorithm is capable to find physically meaningful designs that are characterised by a distribution of the material that minimise the thermal strains as well as the intensity of the applied thermal source by fulfilling the constraint on the volume fraction.

Prospects for the present approach include the extension to the simultaneous optimisation of the topology and anisotropy fields descriptors, taking into account non-linear behaviours and fatigue phenomena. Research on these aspects is ongoing.

CRediT authorship contribution statement

Elisabetta Urso: Writing – original draft, Validation, Software, Methodology, Investigation, Formal analysis. **Marco Montemurro:** Writing – review & editing, Writing – original draft, Validation, Supervision, Software, Methodology, Investigation, Funding acquisition, Formal analysis, Conceptualization.

Declaration of competing interest

The authors declare that they have no known competing financial interests or personal relationships that could have appeared to influence the work reported in this paper.

Data availability

The raw/processed data required to reproduce these findings cannot be shared at this time as the data also forms part of an ongoing study.

Acknowledgements

E. Urso is grateful to French National Research Agency for supporting this work through the research project GLAMOUR-VSC (Global-LocAl

two-level Multi-scale optimisation strategy accOUnting for pRocess-induced singularities to design Variable Stiffness Composites) ANR-21-CE10-0014.

Appendix A. Gradient of the generalised compliance for thermomechanical analyses

The logical steps to find the main result of Proposition 2.1 are presented in this section.

Proof. Considering both the thermal and mechanical equilibrium systems of Eqs. (9) and (16), respectively, the generalised compliance of Eq. (27) can be reformulated as:

$$\begin{aligned} C = {} & \mathbf{f}^{\mathrm{T}}\mathbf{u} - \mathbf{u}_{\mathrm{BC}}^{\mathrm{T}}\mathbf{r} + \boldsymbol{\eta}^{\mathrm{T}}(\mathbf{K}\mathbf{u} + \mathbf{K}_{\mathrm{BC}}\mathbf{u}_{\mathrm{BC}} - \mathbf{f}) + \boldsymbol{\zeta}^{\mathrm{T}}(\mathbf{K}_{\mathrm{BC}}^{\mathrm{T}}\mathbf{u} + \tilde{\mathbf{K}}\mathbf{u}_{\mathrm{BC}} \\ & - \mathbf{r}) + \boldsymbol{\lambda}^{\mathrm{T}}(\mathbf{K}_{\theta}\boldsymbol{\theta} + \mathbf{K}_{\theta\mathrm{BC}}\boldsymbol{\theta}_{\mathrm{BC}} - \boldsymbol{\psi}) + \boldsymbol{\mu}^{\mathrm{T}}(\mathbf{K}_{\theta\mathrm{BC}}^{\mathrm{T}}\boldsymbol{\theta} + \tilde{\mathbf{K}}_{\theta}\boldsymbol{\theta}_{\mathrm{BC}} - \boldsymbol{\psi}_{\mathrm{BC}}), \end{aligned} \tag{A.1}$$

where $\boldsymbol{\eta} \in \mathbb{R}^{N_{\mathrm{DOF}}}$, $\boldsymbol{\zeta} \in \mathbb{R}^{N_{\mathrm{BC}}}$, $\boldsymbol{\lambda} \in \mathbb{R}^{N_{\mathrm{DOF}_\theta}}$, $\boldsymbol{\mu} \in \mathbb{R}^{N_{\mathrm{BC}_\theta}}$ are four arbitrary vectors. Under the hypothesis that the prescribed temperatures $\boldsymbol{\theta}_{\mathrm{BC}}$ and displacements $\mathbf{u}_{\mathrm{BC}}$ do not depend on the topological variables, i.e.,

$$\frac{\partial \mathbf{u}_{\mathrm{BC}}}{\partial \xi_{ij}} = \mathbf{0}, \ \frac{\partial \boldsymbol{\theta}_{\mathrm{BC}}}{\partial \xi_{ij}} = \mathbf{0}, \tag{A.2}$$

the derivative of Eq. (A.1) reads:

$$\begin{aligned} \frac{\partial C}{\partial \xi_{ij}} = {} & \mathbf{u}^{\mathrm{T}}\frac{\partial \mathbf{f}_{\hat{\theta}}}{\partial \xi_{ij}} + \mathbf{f}^{\mathrm{T}}\frac{\partial \mathbf{u}}{\partial \xi_{ij}} - \mathbf{u}_{\mathrm{BC}}^{\mathrm{T}}\frac{\partial \mathbf{r}}{\partial \xi_{ij}} \\ & + \boldsymbol{\eta}^{\mathrm{T}}\left(\frac{\partial \mathbf{K}}{\partial \xi_{ij}}\mathbf{u} + \mathbf{K}\frac{\partial \mathbf{u}}{\partial \xi_{ij}} + \frac{\partial \mathbf{K}_{\mathrm{BC}}}{\partial \xi_{ij}}\mathbf{u}_{\mathrm{BC}} - \frac{\partial \mathbf{f}_{\hat{\theta}}}{\partial \xi_{ij}}\right) \\ & + \boldsymbol{\zeta}^{\mathrm{T}}\left(\frac{\partial \mathbf{K}_{\mathrm{BC}}^{\mathrm{T}}}{\partial \xi_{ij}}\mathbf{u} + \mathbf{K}_{\mathrm{BC}}^{\mathrm{T}}\frac{\partial \mathbf{u}}{\partial \xi_{ij}} + \frac{\partial \tilde{\mathbf{K}}}{\partial \xi_{ij}}\mathbf{u}_{\mathrm{BC}} - \frac{\partial \mathbf{r}}{\partial \xi_{ij}}\right) \\ & + \boldsymbol{\lambda}^{\mathrm{T}}\left(\frac{\partial \mathbf{K}_{\theta}}{\partial \xi_{ij}}\boldsymbol{\theta} + \mathbf{K}_{\theta}\frac{\partial \boldsymbol{\theta}}{\partial \xi_{ij}} + \frac{\partial \mathbf{K}_{\theta\mathrm{BC}}}{\partial \xi_{ij}}\boldsymbol{\theta}_{\mathrm{BC}} - \frac{\partial \boldsymbol{\psi}_{\mathrm{DD}}}{\partial \xi_{ij}}\right) \\ & + \boldsymbol{\mu}^{\mathrm{T}}\left(\frac{\partial \mathbf{K}_{\theta\mathrm{BC}}^{\mathrm{T}}}{\partial \xi_{ij}}\boldsymbol{\theta} + \mathbf{K}_{\theta\mathrm{BC}}^{\mathrm{T}}\frac{\partial \boldsymbol{\theta}}{\partial \xi_{ij}} + \frac{\partial \tilde{\mathbf{K}}_{\theta}}{\partial \xi_{ij}}\boldsymbol{\theta}_{\mathrm{BC}} - \frac{\partial \boldsymbol{\psi}_{\mathrm{BC}}}{\partial \xi_{ij}}\right). \end{aligned} \tag{A.3}$$

In the above equation the term $\frac{\partial \mathbf{f}_{\hat{\theta}}}{\partial \xi_{ij}}$ can be computed by considering Eqs. (21) and (24):

$$\begin{aligned} \frac{\partial \mathbf{f}_{\hat{\theta}}}{\partial \xi_{ij}} &= \sum_{e=1}^{N_e}\frac{1}{\phi_{\theta e}}\frac{\partial \phi_{\theta e}}{\partial \xi_{ij}}\phi_{\theta e}\mathbf{L}_e^{\mathrm{T}}\mathbf{f}_{\hat{\theta}e} + \sum_{e=1}^{N_e}\phi_{\theta e}\mathbf{L}_e^{\mathrm{T}}\hat{\mathbf{a}}_e\frac{\partial \hat{\boldsymbol{\theta}}}{\partial \xi_{ij}} \\ &= \sum_{e\in S_j}\frac{1}{\phi_{\theta e}}\frac{\partial \phi_{\theta e}}{\partial \rho_e}\frac{\partial \rho_e}{\partial \xi_{ij}}\phi_{\theta e}\mathbf{L}_e^{\mathrm{T}}\mathbf{f}_{\hat{\theta}e} \\ &\quad + \sum_{e=1}^{N_e}\phi_{\theta e}\mathbf{L}_e^{\mathrm{T}}\left[\Re(\hat{\mathbf{a}}_e, \varnothing, I_{\theta\mathrm{BC}})\frac{\partial \boldsymbol{\theta}}{\partial \xi_{ij}} + \Re(\hat{\mathbf{a}}_e, \varnothing, I_{\theta})\frac{\partial \boldsymbol{\theta}_{\mathrm{BC}}}{\partial \xi_{ij}}\right] \\ &= \sum_{e\in S_j}\frac{1}{\phi_{\theta e}}\frac{\partial \phi_{\theta e}}{\partial \rho_e}\frac{\partial \rho_e}{\partial \xi_{ij}}\phi_{\theta e}\mathbf{L}_e^{\mathrm{T}}\mathbf{f}_{\hat{\theta}e} + \sum_{e=1}^{N_e}\phi_{\theta e}\mathbf{L}_e^{\mathrm{T}}\mathbf{a}_e\frac{\partial \boldsymbol{\theta}}{\partial \xi_{ij}}, \end{aligned} \tag{A.4}$$

where $\mathbf{a}_e$ can be obtained from Eqs. (33) and (25). By injecting Eq. (A.4) in Eq. (A.3) and by considering Eq. (30), the gradient of the generalised compliance can be expressed as:

$$\begin{aligned} \frac{\partial C}{\partial \xi_{ij}} = {} & \sum_{e\in S_j}\frac{1}{\phi_{\theta e}}\frac{\partial \phi_{\theta e}}{\partial \rho_e}\frac{\partial \rho_e}{\partial \xi_{ij}}w_{\theta_e}^{\mathrm{ext}} + \sum_{e=1}^{N_e}\phi_{\theta_e}\mathbf{u}_e^{\mathrm{T}}\mathbf{a}_e\frac{\partial \boldsymbol{\theta}}{\partial \xi_{ij}} + \mathbf{f}^{\mathrm{T}}\frac{\partial \mathbf{u}}{\partial \xi_{ij}} - \mathbf{u}_{\mathrm{BC}}^{\mathrm{T}}\frac{\partial \mathbf{r}}{\partial \xi_{ij}} \\ & + \boldsymbol{\eta}^{\mathrm{T}}\Bigg(\frac{\partial \mathbf{K}}{\partial \xi_{ij}}\mathbf{u} + \mathbf{K}\frac{\partial \mathbf{u}}{\partial \xi_{ij}} + \frac{\partial \mathbf{K}_{\mathrm{BC}}}{\partial \xi_{ij}}\mathbf{u}_{\mathrm{BC}} - \sum_{e\in S_j}\frac{1}{\phi_{\theta e}}\frac{\partial \phi_{\theta e}}{\partial \rho_e}\frac{\partial \rho_e}{\partial \xi_{ij}}\phi_{\theta e}\mathbf{L}_e^{\mathrm{T}}\mathbf{f}_{\hat{\theta}e} \\ & - \sum_{e=1}^{N_e}\phi_{\theta e}\mathbf{L}_e^{\mathrm{T}}\mathbf{a}_e\frac{\partial \boldsymbol{\theta}}{\partial \xi_{ij}}\Bigg) \\ & + \boldsymbol{\zeta}^{\mathrm{T}}\left(\frac{\partial \mathbf{K}_{\mathrm{BC}}^{\mathrm{T}}}{\partial \xi_{ij}}\mathbf{u} + \mathbf{K}_{\mathrm{BC}}^{\mathrm{T}}\frac{\partial \mathbf{u}}{\partial \xi_{ij}} + \frac{\partial \tilde{\mathbf{K}}}{\partial \xi_{ij}}\mathbf{u}_{\mathrm{BC}} - \frac{\partial \mathbf{r}}{\partial \xi_{ij}}\right) \\ & + \boldsymbol{\lambda}^{\mathrm{T}}\left(\frac{\partial \mathbf{K}_{\theta}}{\partial \xi_{ij}}\boldsymbol{\theta} + \mathbf{K}_{\theta}\frac{\partial \boldsymbol{\theta}}{\partial \xi_{ij}} + \frac{\partial \mathbf{K}_{\theta\mathrm{BC}}}{\partial \xi_{ij}}\boldsymbol{\theta}_{\mathrm{BC}} - \frac{\partial \boldsymbol{\psi}_{\mathrm{DD}}}{\partial \xi_{ij}}\right) \\ & + \boldsymbol{\mu}^{\mathrm{T}}\left(\frac{\partial \mathbf{K}_{\theta\mathrm{BC}}^{\mathrm{T}}}{\partial \xi_{ij}}\boldsymbol{\theta} + \mathbf{K}_{\theta\mathrm{BC}}^{\mathrm{T}}\frac{\partial \boldsymbol{\theta}}{\partial \xi_{ij}} + \frac{\partial \tilde{\mathbf{K}}_{\theta}}{\partial \xi_{ij}}\boldsymbol{\theta}_{\mathrm{BC}} - \frac{\partial \boldsymbol{\psi}_{\mathrm{BC}}}{\partial \xi_{ij}}\right). \end{aligned} \tag{A.5}$$

The adjoint vectors $\boldsymbol{\eta}$, $\boldsymbol{\zeta}$, $\boldsymbol{\lambda}$, $\boldsymbol{\mu}$ are chosen such that the terms multiplying $\frac{\partial \mathbf{u}}{\partial \xi_{ij}}$, $\frac{\partial \boldsymbol{\theta}}{\partial \xi_{ij}}$, $\frac{\partial \mathbf{r}}{\partial \xi_{ij}}$, $\frac{\partial \boldsymbol{\psi}_{\mathrm{BC}}}{\partial \xi_{ij}}$ vanish, i.e.,

$$\boldsymbol{\mu}^{\mathrm{T}} = \mathbf{0} \ \rightarrow \ \boldsymbol{\mu} = \mathbf{0}, \tag{A.6}$$

$$-\mathbf{u}_{\mathrm{BC}}^{\mathrm{T}} - \boldsymbol{\zeta}^{\mathrm{T}} = \mathbf{0} \ \rightarrow \ \boldsymbol{\zeta} = -\mathbf{u}_{\mathrm{BC}}, \tag{A.7}$$

$$\mathbf{f}^{\mathrm{T}} + \boldsymbol{\eta}^{\mathrm{T}}\mathbf{K} + \boldsymbol{\zeta}^{\mathrm{T}}\mathbf{K}_{\mathrm{BC}}^{\mathrm{T}} = \mathbf{0} \ \rightarrow \ \mathbf{K}\boldsymbol{\eta} = \mathbf{K}_{\mathrm{BC}}\mathbf{u}_{\mathrm{BC}} - \mathbf{f} = -\mathbf{K}\mathbf{u} \ \rightarrow \ \boldsymbol{\eta} = -\mathbf{u}, \tag{A.8}$$

$$\begin{aligned} & \sum_{e=1}^{N_e}\phi_{\theta_e}\mathbf{u}_e^{\mathrm{T}}\mathbf{a}_e - \boldsymbol{\eta}^{\mathrm{T}}\sum_{e=1}^{N_e}\phi_{\theta_e}\mathbf{L}_e^{\mathrm{T}}\mathbf{a}_e + \boldsymbol{\lambda}^{\mathrm{T}}\mathbf{K}_{\theta} = \mathbf{0} \ \rightarrow \\ & \rightarrow \ \boldsymbol{\lambda}^{\mathrm{T}}\mathbf{K}_{\theta} = -2\sum_{e=1}^{N_e}\phi_{\theta_e}\mathbf{u}_e^{\mathrm{T}}\mathbf{a}_e \ \rightarrow \end{aligned} \tag{A.9}$$

$$\mathbf{K}_{\theta}\boldsymbol{\lambda} = -2\sum_{e=1}^{N_e}\phi_{\theta_e}\mathbf{a}_e^{\mathrm{T}}\mathbf{u}_e = \mathbf{d} \text{ (from Eq. (32))}.$$

By injecting Eqs. (A.6)-(A.9) in Eq. (A.5), the generalised compliance partial derivative becomes:

$$\begin{aligned} \frac{\partial C}{\partial \xi_{ij}} = {} & \sum_{e\in S_j}\frac{2}{\phi_{\theta e}}\frac{\partial \phi_{\theta e}}{\partial \rho_e}\frac{\partial \rho_e}{\partial \xi_{ij}}w_{\theta_e}^{\mathrm{ext}} - \mathbf{u}^{\mathrm{T}}\frac{\partial \mathbf{K}}{\partial \xi_{ij}}\mathbf{u} - 2\mathbf{u}^{\mathrm{T}}\frac{\partial \mathbf{K}_{\mathrm{BC}}^{\mathrm{T}}}{\partial \xi_{ij}}\mathbf{u}_{\mathrm{BC}} \\ & - \mathbf{u}_{\mathrm{BC}}^{\mathrm{T}}\frac{\partial \tilde{\mathbf{K}}}{\partial \xi_{ij}}\mathbf{u}_{\mathrm{BC}} + \boldsymbol{\lambda}^{\mathrm{T}}\left(\frac{\partial \mathbf{K}_{\theta}}{\partial \xi_{ij}}\boldsymbol{\theta} + \frac{\partial \mathbf{K}_{\theta\mathrm{BC}}}{\partial \xi_{ij}}\boldsymbol{\theta}_{\mathrm{BC}} - \frac{\partial \boldsymbol{\psi}_{\mathrm{DD}}}{\partial \xi_{ij}}\right). \end{aligned} \tag{A.10}$$

As demonstrated in [46], the following equality holds:

$$\begin{aligned} & \mathbf{u}^{\mathrm{T}}\frac{\partial \mathbf{K}}{\partial \xi_{ij}}\mathbf{u} + 2\mathbf{u}^{\mathrm{T}}\frac{\partial \mathbf{K}_{\mathrm{BC}}^{\mathrm{T}}}{\partial \xi_{ij}}\mathbf{u}_{\mathrm{BC}} + \mathbf{u}_{\mathrm{BC}}^{\mathrm{T}}\frac{\partial \tilde{\mathbf{K}}}{\partial \xi_{ij}}\mathbf{u}_{\mathrm{BC}} = \hat{\mathbf{u}}^{\mathrm{T}}\frac{\partial \hat{\mathbf{K}}}{\partial \xi_{ij}}\hat{\mathbf{u}} \\ & = \sum_{e\in S_j}\frac{1}{\phi_{Ke}}\frac{\partial \phi_{Ke}}{\partial \rho_e}\frac{\partial \rho_e}{\partial \xi_{ij}}w_e, \end{aligned} \tag{A.11}$$

where w_e has been defined in Eq. (29). Consequently, Eq. (A.10) can be simplified to:

$$\begin{aligned} \frac{\partial C}{\partial \xi_{ij}} = {} & \sum_{e\in S_j}\frac{\partial \rho_e}{\partial \xi_{ij}}\left(\frac{2}{\phi_{\theta e}}\frac{\partial \phi_{\theta e}}{\partial \rho_e}w_{\theta e}^{\mathrm{ext}} - \frac{1}{\phi_{Ke}}\frac{\partial \phi_{Ke}}{\partial \rho_e}w_e\right) \\ & + \boldsymbol{\lambda}^{\mathrm{T}}\left(\frac{\partial \mathbf{K}_{\theta}}{\partial \xi_{ij}}\boldsymbol{\theta} + \frac{\partial \mathbf{K}_{\theta\mathrm{BC}}}{\partial \xi_{ij}}\boldsymbol{\theta}_{\mathrm{BC}} - \frac{\partial \boldsymbol{\psi}_{\mathrm{DD}}}{\partial \xi_{ij}}\right). \end{aligned} \tag{A.12}$$

In the above formula, the terms multiplying $\boldsymbol{\lambda}^{\mathrm{T}}$ simplifies to:

$$\begin{aligned} & \boldsymbol{\lambda}^{\mathrm{T}}\frac{\partial \mathbf{K}_{\theta}}{\partial \xi_{ij}}\boldsymbol{\theta} + \boldsymbol{\lambda}^{\mathrm{T}}\frac{\partial \mathbf{K}_{\theta\mathrm{BC}}}{\partial \xi_{ij}}\boldsymbol{\theta}_{\mathrm{BC}} - \boldsymbol{\lambda}^{\mathrm{T}}\frac{\partial \boldsymbol{\psi}_{\mathrm{DD}}}{\partial \xi_{ij}} \\ & = \boldsymbol{\lambda}^{\mathrm{T}}\left[\Re\left(\frac{\partial \hat{\mathbf{K}}_{\theta}}{\partial \xi_{ij}}, I_{\theta\mathrm{BC}}, I_{\theta\mathrm{BC}}\right)\boldsymbol{\theta} + \Re\left(\frac{\partial \hat{\mathbf{K}}_{\theta}}{\partial \xi_{ij}}, I_{\theta\mathrm{BC}}, I_{\theta}\right)\boldsymbol{\theta}_{\mathrm{BC}} - \frac{\partial \boldsymbol{\psi}_{\mathrm{DD}}}{\partial \xi_{ij}}\right] \\ & = \boldsymbol{\lambda}^{\mathrm{T}}\sum_{e\in S_j}\frac{1}{\phi_{K_{\theta e}}}\frac{\partial \phi_{K_{\theta e}}}{\partial \rho_e}\frac{\partial \rho_e}{\partial \xi_{ij}}\phi_{K_{\theta e}}\Re\left(\hat{\mathbf{L}}_{\theta e}^{\mathrm{T}}, I_{\theta\mathrm{BC}}, \varnothing\right)\left[\mathbf{K}_{\theta e}\Re\left(\hat{\mathbf{L}}_{\theta e}, \varnothing, I_{\theta\mathrm{BC}}\right)\boldsymbol{\theta}\right. \\ & \quad \left. + \mathbf{K}_{\theta e}\Re\left(\hat{\mathbf{L}}_{\theta e}, \varnothing, I_{\theta}\right)\boldsymbol{\theta}_{\mathrm{BC}}\right] \\ & \quad - \boldsymbol{\lambda}^{\mathrm{T}}\sum_{e\in S_j}\frac{\partial \phi_{\psi e}}{\partial \rho_e}\frac{\partial \rho_e}{\partial \xi_{ij}}\Re\left(\hat{\mathbf{L}}_{\theta e}^{\mathrm{T}}, I_{\theta\mathrm{BC}}, \varnothing\right)\boldsymbol{\psi}_{\mathrm{DD}e}^{0} \\ & = \boldsymbol{\lambda}^{\mathrm{T}}\sum_{e\in S_j}\frac{1}{\phi_{K_{\theta e}}}\frac{\partial \phi_{K_{\theta e}}}{\partial \rho_e}\frac{\partial \rho_e}{\partial \xi_{ij}}\phi_{K_{\theta e}}\mathbf{L}_{\theta e}^{\mathrm{T}}\mathbf{K}_{\theta e}\hat{\mathbf{L}}_{\theta e}\hat{\boldsymbol{\theta}} \end{aligned}$$

$$
- \lambda^{\mathrm{T}} \sum_{e \in S_j} \frac{\partial \phi_{\psi e}}{\partial \rho_e} \frac{\partial \rho_e}{\partial \xi_{ij}} \mathbf{L}_{\theta e}^{\mathrm{T}} \boldsymbol{\psi}_{\mathrm{DD}e}^{0}
$$

$$
= \sum_{e \in S_j} \frac{\partial \rho_e}{\partial \xi_{ij}} \left(\frac{1}{\phi_{K_{\theta e}}} \frac{\partial \phi_{K_{\theta e}}}{\partial \rho_e} \lambda_e^{\mathrm{T}} \boldsymbol{\psi}_e - \frac{\partial \phi_{\psi e}}{\partial \rho_e} \lambda_e^{\mathrm{T}} \boldsymbol{\psi}_{\mathrm{DD}e}^{0} \right). \tag{A.13}
$$

where $\boldsymbol{\psi}_e$ is provided in Eq. (31). By injecting Eq. (A.13) in Eq. (A.12) one obtains Eq. (28) and this last passage ends the proof. ■

References

[1] Bendsøe MP, Sigmund O. Topology optimization. Berlin, Heidelberg: Springer Berlin Heidelberg; 2004.

[2] Bendsøe MP, Kikuchi N. Generating optimal topologies in structural design using a homogenization method. Comput Methods Appl Mech Eng 1988;71(2):197–224.

[3] Allaire G, Jouve F, Toader A-M. Structural optimization using sensitivity analysis and a level-set method. J Comput Phys 2004;194(1):363–93.

[4] Wang MY, Wang X, Guo D. A level set method for structural topology optimization. Comput Methods Appl Mech Eng 2003;192(1):227–46.

[5] Zheng J, Zhu S, Soleymani F. A new efficient parametric level set method based on radial basis function-finite difference for structural topology optimization. Comput Struct 2024;297:107364.

[6] Bendsoe MP, Sigmund O. Topology optimization: theory, methods, and applications. Springer Science & Business Media; 2003.

[7] Stolpe M, Svanberg K. An alternative interpolation scheme for minimum compliance topology optimization. Struct Multidiscip Optim 2001;22(2):116–24.

[8] Sigmund O. Morphology-based black and white filters for topology optimization. Struct Multidiscip Optim 2007;33(4–5):401–24.

[9] Lazarov BS, Sigmund O. Filters in topology optimization based on Helmholtz-type differential equations. Int J Numer Methods Eng 2011;86(6):765–81.

[10] Bézier P. Courbes et surfaces. Paris: Springer-Verlag/Hermès; 1986.

[11] Farin GE. Curves and surfaces for CAGD: a practical guide. In: Morgan Kaufmann series in computer graphics and geometric modeling. 5th edition. San Francisco, CA: Morgan Kaufmann; 2001.

[12] Piegl L, Tiller W. The NURBS book. In: Monographs in visual communications. Berlin, Heidelberg: Springer; 1995.

[13] Costa G, Montemurro M, Pailhès J. A 2D topology optimisation algorithm in NURBS framework with geometric constraints. Int J Mech Mater Des 2018;14:669–96.

[14] Costa G, Montemurro M, Pailhès J. NURBS hyper-surfaces for 3D topology optimization problems. Mech Adv Mat Struct 2021;28(7):665–84.

[15] Bertolino G, Montemurro M, Perry N, Pourroy F. An efficient hybrid optimisation strategy for surface reconstruction. Comput Graph Forum 2021;40(6):215–41.

[16] Bruyneel M, Duysinx P. Note on topology optimization of continuum structures including self weight. Struct Multidiscip Optim 2005;29:245–56.

[17] Tamijani AY. Stress and stiffness-based topology optimization of two-material thermal structures. Comput Struct 2021;256:106641.

[18] Ogawa S, Yamada T. Stress constraint topology optimization of coupled thermo-mechanical problems using the temperature dependence of allowable stress. Comput Struct 2023;281:107006.

[19] Kambampati S, Gray JS, Kim H Alicia. Level set topology optimization of structures under stress and temperature constraints. Comput Struct 2020;235:106265.

[20] Shishir MIR, Tabarraei A. Multi–materials topology optimization using deep neural network for coupled thermo–mechanical problems. Comput Struct 2024;291:107218.

[21] Cho S, Choi J-Y. Efficient topology optimization of thermo-elasticity problems using coupled field adjoint sensitivity analysis method. Finite Elem Anal Des 2005;41(15):1481–95.

[22] Álvarez Hostos JC, Fachinotti VD, Peralta I. Computational design of thermo-mechanical metadevices using topology optimization. Appl Math Model 2021;90:758–76.

[23] Zhang W, Yang J, Xu Y, Gao T. Topology optimization of thermoelastic structures: mean compliance minimization or elastic strain energy minimization. Struct Multidiscip Optim 2014;49:417–29.

[24] Sigmund O. A 99 line topology optimization code written in Matlab. Struct Multidiscip Optim 2001;21(2):120–7.

[25] Li Q, Steven GP, Xie Y. Displacement minimization of thermoelastic structures by evolutionary thickness design. Comput Methods Appl Mech Eng 1999;179(3–4):361–78.

[26] Li Q, Steven GP, Xie YM, Querin OM. Evolutionary topology optimization for temperature reduction of heat conducting fields. Int J Heat Mass Transf 2004;47(23):5071–83.

[27] Haslinger J, Hillebrand A, Kärkkäinen T, Miettinen M. Optimization of conducting structures by using the homogenization method. Struct Multidiscip Optim 2002;24(2):125–40.

[28] Gersborg-Hansen A, Bendsøe MP, Sigmund O. Topology optimization of heat conduction problems using the finite volume method. Struct Multidiscip Optim 2006;31(4):251–9.

[29] Munk DJ, Verstraete D, Vio GA. Effect of fluid-thermal–structural interactions on the topology optimization of a hypersonic transport aircraft wing. J Fluids Struct 2017;75:45–76.

[30] Zhuang C, Xiong Z. Temperature-constrained topology optimization of transient heat conduction problems. Numer Heat Transf, Part B, Fundam 2015;68(4):366–85.

[31] Zhu X, Zhao C, Wang X, Zhou Y, Hu P, Ma Z. Temperature-constrained topology optimization of thermo-mechanical coupled problems. Eng Optim 2019;51:1–23.

[32] Ooms T, Vantyghem G, Thienpont T, Van Coile R, De Corte W. Compliance-based topology optimization of structural components subjected to thermo-mechanical loading. Struct Multidiscip Optim 2023;66(6):24.

[33] Gao T, Zhang W. Topology optimization involving thermo-elastic stress loads. Struct Multidiscip Optim 2010;42:725–38.

[34] Pedersen P, Pedersen N. Strength optimized designs of thermoelastic structures. Struct Multidiscip Optim 2010;42:681–91.

[35] Pedersen P, Pedersen NL. Design objectives with non-zero prescribed support displacements. Struct Multidiscip Optim 2011;43(2):205–14.

[36] Deaton JD, Grandhi RV. Stress-based design of thermal structures via topology optimization. Struct Multidiscip Optim 2016;53(2):253–70.

[37] van de Ven E, Hooijkamp E, Langelaar M, van Keulen F. Topology optimization of a transient thermo-mechanical problem using material penalization. In: 11th world congress on structural and multidisciplinary optimization; 2015.

[38] Takezawa A, Yoon GH, Jeong SH, Kobashi M, Kitamura M. Structural topology optimization with strength and heat conduction constraints. Comput Methods Appl Mech Eng 2014;276:341–61.

[39] Gao T, Zhang W, Zhu J. Structural topology optimization under inertial loads. Lixue Xuebao/Chin J Theor Appl Mech 2009;41:530–41.

[40] Xia Q, Wang MY. Topology optimization of thermoelastic structures using level set method. Comput Mech 2008;42(6):837–57.

[41] Deng S, Suresh K. Stress constrained thermo-elastic topology optimization with varying temperature fields via augmented topological sensitivity based level-set. Struct Multidiscip Optim 2017;56(6):1413–27.

[42] Liu K, Tovar A. An efficient 3D topology optimization code written in Matlab. Struct Multidiscip Optim 2014;50(6):1175–96.

[43] Zhan J, Li J, Liu P, Luo Y. A gradient-free topology optimization strategy for continuum structures with design-dependent boundary loads. Symmetry 2021;13(11):1976.

[44] Zhang H, Liu S, Zhang X. Topology optimization of continuum structures subjected to self weight loads. Chin J Theor Appl Mech 2009;41(1):98–104.

[45] Fang L, Wang X, Zhou H. Topology optimization of thermoelastic structures using MMV method. Appl Math Model 2022;103:604–18.

[46] Montemurro M. On the structural stiffness maximisation of anisotropic continua under inhomogeneous Neumann-Dirichlet boundary conditions. Compos Struct 2022;287:115289.

[47] Roiné T, Montemurro M, Pailhès J. Stress-based topology optimization through non-uniform rational basis spline hyper-surfaces. Mech Adv Mat Struct 2022;29(23):3387–407.

[48] Costa G, Montemurro M, Pailhès J. Minimum length scale control in a NURBS-based SIMP method. Comput Methods Appl Mech Eng 2019;354:963–89.

[49] Eschenauer HA, Olhoff N. Topology optimization of continuum structures: a review. Appl Mech Rev 2001;54(4):331–90.

[50] Urso E, Zerrouq S-e, Montemurro M. A topology optimization method for problems with design-dependent loads based on non-uniform rational basis spline entities. Mech Adv Mat Struct 2023:1–16. https://doi.org/10.1080/15376494.2023.2294495.

[51] Svanberg K. A class of globally convergent optimization methods based on conservative convex separable approximations. SIAM J Optim 2002;12(2):555–73. https://doi.org/10.1137/S1052623499362822. http://epubs.siam.org/doi/10.1137/S1052623499362822.

[52] ANSYS, Inc., 275 Technology Drive, Canonsburg, PA 15317. ANSYS mechanical APDL modeling and meshing guide; 2022.

[53] Rodrigues H, Fernandes P. A material based model for topology optimization of thermoelastic structures. Int J Numer Methods Eng 1995;38(12):1951–65. https://doi.org/10.1002/nme.1620381202. _eprint: https://onlinelibrary.wiley.com/doi/pdf/10.1002/nme.1620381202.